



## Adhesion of bubbles and drops to solid surfaces, and anisotropic surface tensions studied by capillary meniscus dynamometry☆



Krassimir D. Danov<sup>a</sup>, Romyana D. Stanimirova<sup>a</sup>, Peter A. Kralchevsky<sup>a,\*</sup>, Krastanka G. Marinova<sup>a</sup>, Simeon D. Stoyanov<sup>b,c,d</sup>, Theodorus B.J. Blijdenstein<sup>b</sup>, Andrew R. Cox<sup>e</sup>, Eddie G. Pelan<sup>b</sup>

<sup>a</sup> Department of Chemical & Pharmaceutical Engineering, Faculty of Chemistry & Pharmacy, Sofia University, Sofia 1164, Bulgaria

<sup>b</sup> Unilever Research & Development Vlaardingen, 3133AT Vlaardingen, The Netherlands

<sup>c</sup> Laboratory of Physical Chemistry and Colloid Science, Wageningen University, 6703 HB Wageningen, The Netherlands

<sup>d</sup> Department of Mechanical Engineering, University College London, WC1E 7JE, UK

<sup>e</sup> Unilever Research & Development, Colworth Science Park, Sharnbrook MK44 1LQ, UK

### ARTICLE INFO

Available online 19 June 2015

#### Keywords:

Foams and emulsions  
Bubble and drop adhesion to walls  
Disjoining pressure vs. transversal tension  
Isotropic and anisotropic interfaces  
Capillary meniscus dynamometry  
Protein and egg yolk solutions

### ABSTRACT

Here, we review the principle and applications of two recently developed methods: the capillary meniscus dynamometry (CMD) for measuring the surface tension of bubbles/drops, and the capillary bridge dynamometry (CBD) for quantifying the bubble/drop adhesion to solid surfaces. Both methods are based on a new data analysis protocol, which allows one to decouple the two components of non-isotropic surface tension. For an axisymmetric non-fluid interface (e.g. bubble or drop covered by a protein adsorption layer with shear elasticity), the CMD determines the two different components of the anisotropic surface tension,  $\sigma_s$  and  $\sigma_\phi$ , which are acting along the “meridians” and “parallels”, and vary throughout the interface. The method uses data for the instantaneous bubble (drop) profile and capillary pressure, but the procedure for data processing is essentially different from that of the conventional drop shape analysis (DSA) method. In the case of bubble or drop pressed against a substrate, which forms a capillary bridge, the CBD method allows one to determine also the capillary-bridge force for both isotropic (fluid) and anisotropic (solidified) adsorption layers. The experiments on bubble (drop) detachment from the substrate show the existence of a maximal pulling force,  $F_{\max}$ , that can be resisted by an adherent fluid particle.  $F_{\max}$  can be used to quantify the strength of adhesion of bubbles and drops to solid surfaces. Its value is determined by a competition of attractive transversal tension and repulsive disjoining pressure forces. The greatest  $F_{\max}$  values have been measured for bubbles adherent to glass substrates in pea-protein solutions. The bubble/wall adhesion is lower in solutions containing the protein HFBII hydrophobin, which could be explained with the effect of sandwiched protein aggregates. The applicability of the CBD method to emulsion systems is illustrated by experiments with soybean-oil drops adherent to hydrophilic and hydrophobic substrates in egg yolk solutions. The results reveal how the interfacial rigidity, as well as the bubble/wall and drop/wall adhesion forces, can be quantified and controlled in relation to optimizing the properties of foams and emulsions.

© 2015 Elsevier B.V. All rights reserved.

### Contents

1.	Introduction . . . . .	224
2.	Theoretical background . . . . .	224
2.1.	Mechanical balance equations for axisymmetric elastic interfacial layers . . . . .	224
2.2.	Computational procedure of the capillary meniscus dynamometry (CMD) . . . . .	226
3.	Experimental setups and materials . . . . .	227
4.	Application of CMD to bubbles and drops . . . . .	227
4.1.	Interfaces with isotropic and anisotropic surface tension . . . . .	227
4.2.	CMD vs. the drop shape analysis (DSA) . . . . .	228
4.3.	Comparison of CMD with other theoretical approaches to anisotropic interfaces . . . . .	229
5.	Capillary bridge dynamometry (CBD) . . . . .	229

☆ This article is dedicated to Prof. Dr. Clayton J. Radke on the occasion of his 70th birthday.

\* Corresponding author. Tel.: +359 2 962 5310; fax: +359 2 962 5643.

E-mail address: [pk@lcpce.uni-sofia.bg](mailto:pk@lcpce.uni-sofia.bg) (P.A. Kralchevsky).

5.1.	Bridge with isotropic surface tension . . . . .	231
5.2.	Bridge with anisotropic surface tension and wrinkles . . . . .	231
5.3.	Bridge with partially isotropic surface tension . . . . .	231
6.	Adhesion force determination from CBD data . . . . .	232
6.1.	Mechanical balances in the adhesion zone of a bubble or drop . . . . .	232
6.2.	Bubble adhesion to surfaces – data analysis . . . . .	233
6.3.	Emulsion drop adhesion to surfaces – data analysis . . . . .	235
7.	Summary and conclusions . . . . .	237
	Acknowledgements . . . . .	238
	References . . . . .	238

## 1. Introduction

In the present article, we review results on the adhesion of bubbles and drops to a solid surface in relation to the interactions of foams and emulsions with the container's wall. The paper is focused on model experiments with a bubble or drop, which is (i) formed on the tip of a capillary tube in an aqueous solution; (ii) pressed to a solid substrate to adhere, and (iii) detached from the substrate to measure the maximal pulling force, which the adherent bubble/drop can withstand. When pressed against the substrate, the fluid particle (bubble, drop) forms a capillary bridge between the solid wall and the capillary. The force of interaction between the fluid particle and the solid surface can be determined from the capillary-bridge force that, in turns, can be found from the meniscus (capillary bridge) shape. For this reason, a central issue in the present article is the determination of the surface tension from the instantaneous meniscus profile.

The above task is not simple, because adsorption layers from proteins [1–10]; phospholipids [11–13]; polymers, polyelectrolytes and their mixtures with proteins [14–16]; saponins [17]; particles [18,19] and asphaltenes [20] often exhibit a complex surface rheology and could possess surface shear elasticity. In the latter case, they behave as a two-dimensional elastic solid (membrane). The stresses acting in such layers are anisotropic and non-uniform – they vary along the interface [21–25]. If a pendant drop or buoyant bubble is covered with such a layer, the components of surface tension acting along the “meridians” and “parallels”,  $\sigma_s$  and  $\sigma_\varphi$ , can be rather different. Then, the conventional drop shape analysis (DSA) method [26], which is based on the presumption of uniform and isotropic surface tension, is inapplicable.

This problem can be overcome by using the recently developed method *capillary meniscus dynamometry* (CMD), which is applicable to anisotropic interfaces and allows one to determine  $\sigma_s$  and  $\sigma_\varphi$  in each interfacial point [27]. The method is based on obtaining and processing experimental data for the digitized drop/bubble profile and for the pressure difference across the meniscus. The CMD computational procedure for determining two surface tensions,  $\sigma_s$  and  $\sigma_\varphi$ , in each interfacial point is essentially different from that used in DSA to determine a single surface tension  $\sigma$  for the whole meniscus.

The first quantitative and methodological studies on profiles of axisymmetric drops were carried out by Bashforth and Adams [28] and Andreas et al. [29]; see Ref. [30] for a detailed review. Using computer image analysis, Neumann et al. [26] automated the pendant drop method by numerical fitting of the digitized drop profile with the Laplace equation of capillarity. This method (DSA) found a wide application for the measurements of static and dynamic surface tension and interfacial rheology [31–33]. Its accuracy was tested in a number of methodological studies [34–36].

If the drop or bubble is small and its gravitational deformation does not allow a sufficiently accurate determination of the surface tension,  $\sigma$ , one can use another method, viz. the capillary pressure tensiometry (CPT), which is based on measurements of the drop/bubble *capillary pressure*. In the first CPT studies, image analysis was not used; instead, in each moment of time the drop radius was calculated from the known volume dosing rate [37–39]. The CPT has different versions

and realizations and was applied for measurements of static and dynamic surface tension and dilatational surface rheology [33,40,41]. CPT and DSA can be assembled in one apparatus, which combines the capabilities of both methods [42–44]. In our measurements reported in the present article, we utilized a DSA apparatus upgraded with a pressure transducer [42], but the data were processed by using the CMD method [27].

The paper is organized as follows. In Section 2, we present the theoretical basis of the CMD method in a more general form, which is applicable not only to pendant drops and buoyant bubbles [27], but also to axisymmetric capillary bridges. Section 3 describes the experimental setups and materials. Section 4 gives a review on the application of CMD to buoyant bubbles and pendant drops. The differences between the CMD and DSA, as well as the relation between CMD and other approaches based on Hookean models of elastic plates [21–25], are discussed. In Section 5, the CMD method is applied to analyze data for the profiles of capillary bridges with isotropic, anisotropic and partially isotropic surface tension. Finally, in Section 6 the mechanical balances in the adhesion zone are analyzed, and the force of bubble/drop adhesion to glass substrates is quantified on the basis of the obtained experimental data.

The experimental material on pendant drops and buoyant bubbles represents a review of previous results, whereas the material on capillary bridges is reported here for the first time.

## 2. Theoretical background

### 2.1. Mechanical balance equations for axisymmetric elastic interfacial layers

The balance of linear momentum in each point of a curved interface between two fluid phases reads [45–47]:

$$\nabla_s \cdot \boldsymbol{\sigma} = p_s \mathbf{n} \quad (1)$$

Here,  $\boldsymbol{\sigma}$  is the tensor of surface tension (the surface stress tensor);  $p_s$  is the local pressure difference across the interface;  $\mathbf{n}$  is its running outer normal (Fig. 1);  $\nabla_s$  is the surface del (gradient) operator; the dot symbolizes divergence. In Eq. (1), inertial and gravitational terms, which are due to the mass of the interfacial layer, are neglected.

Here, we will consider axisymmetric menisci, like the surface of a pendant drop (Fig. 1a), or a capillary bridge (Fig. 1b). Cylindrical coordinates  $(r, \varphi, z)$  will be used, with coordinate origin as shown in Fig. 1a and b;  $r$  is the radial coordinate and  $\varphi$  is the azimuthal angle. The generatrix of the meniscus profile can be parameterized with the length of the arc,  $s$ . In view of the axial symmetry, the matrix of the surface stress tensor is diagonal in the selected coordinate system:

$$\boldsymbol{\sigma} = \begin{pmatrix} \sigma_s & 0 \\ 0 & \sigma_\varphi \end{pmatrix} \quad (2)$$

where  $\sigma_s$  and  $\sigma_\varphi$  are the surface tensions acting tangentially to the  $s$  and  $\varphi$  coordinate lines, i.e. along the “meridians” and “parallels”,

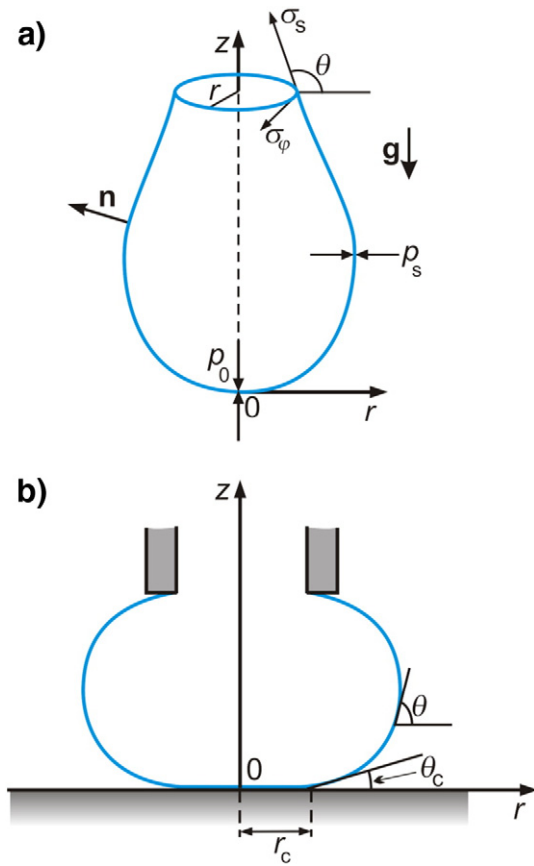


**Fig. 1.** (a) Sketch of a pendant drop;  $\sigma_s$  and  $\sigma_\varphi$  are two components of surface tension acting along the “meridians” and “parallels”. The vertical resultant of the surface tension force,  $2\pi r\sigma_s \sin\theta$ , is counterbalanced by the pressure force  $F_p$ ; see Eqs. (10) and (13). (b) Capillary bridge formed by a drop or bubble, which has been created at the tip of a capillary tube and pressed against a solid surface;  $r_c$  and  $\theta_c$  are the contact radius and angle.

respectively (Fig. 1a). In view of Eq. (2), the projections of the vectorial Eq. (1) along the “meridians” and along  $\mathbf{n}$  read:

$$\sigma_\varphi = \frac{d}{dr}(\sigma_s r) \quad (\text{tangential projection}) \quad (3)$$

$$\kappa_s \sigma_s + \kappa_\varphi \sigma_\varphi = p_s \quad (\text{normal projection}) \quad (4)$$

where  $\kappa_s$  and  $\kappa_\varphi$  are the respective two principal curvatures:

$$\kappa_s = \frac{d \sin \theta}{dr} \quad \text{and} \quad \kappa_\varphi = \frac{\sin \theta}{r} \quad (5)$$

$\theta$  is the running meniscus slope angle ( $\tan \theta = dz/dr$ ). Eq. (4) is a generalization of the Laplace equation of capillarity for anisotropic interfaces. The third projection of Eq. (1), along the  $\varphi$ -lines (“parallels”), is trivial because of the axial symmetry. The detailed derivation of Eqs. (3) and (4) can be found, e.g., in Appendix B of Ref. [27].

Here, we consider only surface tensions acting tangentially to the interface (membrane). In the case of objects of high curvature and low membrane tensions, the transverse components of  $\sigma$  and the related interfacial bending moments (torques) should be taken into account [11,46,47]. The bending-moment effects are out of the scope of the present study, because here we are dealing with millimeter-sized drops, bubbles and capillary bridges with relatively low surface curvature.

If the surface tension is uniform ( $d\sigma_s/dr = 0$ ), Eq. (3) reduces to  $\sigma_\varphi = \sigma_s$ . In other words, if the surface tension is *uniform*, the balance of the linear momentum implies that it is also *isotropic*:  $\sigma_\varphi = \sigma_s = \sigma$ .

This statement can be generalized to an arbitrarily curved interface with symmetric surface stress tensor, viz. if the surface stresses are isotropic, they are also uniform throughout the interface, and *vice versa*. The proof can be found in Appendix A of Ref. [27].

A substitution of  $\sigma_\varphi$ ,  $\kappa_s$  and  $\kappa_\varphi$  from Eqs. (3) and (5) into Eq. (4), after some transformations yields:

$$\frac{d}{dr}(r\sigma_s \sin \theta) = p_s r \quad (6)$$

An alternative derivation of Eq. (6) by balancing the forces acting on an elementary segment of the axisymmetric meniscus can be found in ref. [27]; see Fig. 1b therein. This relatively simple derivation shows how elastic membranes, which allow different radii of curvature and non-spherical shapes, can be in equilibrium with bulk phases of isotropic pressure. For the more general case of anisotropic bulk pressure tensors and dynamic processes, force balance derivation of the basic equations can be found in Ref. [46]; see Fig. 1 therein. If  $\sigma_s$  is constant (independent of  $r$ ), then Eq. (6) reduces to the conventional Laplace equation of capillarity [26,46,47].

Taking into account the effect of the gravitational hydrostatic pressure, we can express  $p_s$  in the form:

$$p_s \equiv p_{\text{in}} - p_{\text{out}} = p_0 - \varepsilon g z \Delta \rho \quad (7)$$

where  $p_0$  is the pressure difference across the meniscus at level  $z = 0$ ;  $\Delta \rho \equiv |\rho_{\text{in}} - \rho_{\text{out}}|$  is the magnitude of the difference between the mass densities of the inner and outer phases;  $g$  is the magnitude of the acceleration due to gravity;  $\varepsilon = 1$  if the gravity elongates the drop/bubble (e.g. pendant drop, buoyant bubble), whereas  $\varepsilon = -1$  in the opposite case (e.g. sessile drop).

For a *capillary bridge* (Fig. 1b), let us integrate Eq. (6), along with Eq. (7), from  $r = r_c$  to an arbitrary  $r$ , and multiply the result by  $2\pi$ :

$$2\pi r \sigma_s \sin \theta = \pi r^2 p_0 - 2\pi \varepsilon g \Delta \rho \int_{r_c}^r \tilde{r} z(\tilde{r}) d\tilde{r} - F \quad (8)$$

where  $\tilde{r}$  is an integration variable;  $p_0$  is the pressure difference between the inner and outer fluid at level  $z = 0$  (just above the upper film surface in the contact zone; see Fig. 1b), and  $F$  is an integration constant:

$$F = \pi r_c^2 p_0 - 2\pi r_c \sigma_c \sin \theta_c \quad (9)$$

Here, by definition,  $\sigma_c$ ,  $r_c$  and  $\theta_c$  are the values of  $\sigma_s$ ,  $r$  and  $\theta$  at  $z = 0$ , i.e. at the contact line. In the case of pendant/buoyant drop or bubble (Fig. 1a) we have:

$$r_c = 0, \quad F = 0 \quad (\text{drop or bubble}) \quad (10)$$

In the more general case ( $r_c > 0$ ),  $F$  is the force acting on the substrate because of the presence of a capillary bridge, i.e. the *capillary bridge force* [47]. The sign of  $F$  in Eq. (9) has been chosen in such a way that  $F < 0$  in the case of *attraction* between the two bodies connected by the capillary bridge, whereas  $F > 0$  in the case of *repulsion*.

The first two terms in the right-hand side of Eq. (8) represent the force,  $F_p$ , due to the pressure difference; for an arbitrary cross-section of radius  $r$ , this force is:

$$F_p \equiv \pi r^2 p_0 + \pi \varepsilon g \Delta \rho (I - r^2 z) \quad (11)$$

$$I = \int_0^z r^2(\tilde{z}) d\tilde{z} \quad (12)$$

In Eq. (11), integration by parts has been used;  $I$  is an integral, which is calculated numerically from the digitized drop profile (see below). In view of Eq. (11), we can represent Eq. (8) in the form:

$$F_p = 2\pi r\sigma_s \sin\theta + F \quad (13)$$

The experiment gives  $p_0$  and the meniscus profile  $r(z)$ . From these data one can determine  $F_p(z)$  and  $\theta(z)$  for each given  $z$ . Then, the local value of the meridional tension  $\sigma_s$  can be calculated from Eq. (13):

$$\sigma_s(z) = \frac{F_p(z) - F}{2\pi r(z) \sin\theta(z)} \quad (14)$$

Next, in view of Eq. (5) the local values of the two principle curvatures are:

$$\kappa_\varphi(z) = \frac{\sin\theta(z)}{r(z)}, \quad \kappa_s(z) = -\frac{d \cos\theta(z)}{dz} \quad (15)$$

where we have used the relation  $dz/dr = \tan\theta$ . The derivative in Eq. (15) can be calculated numerically, as explained in Section 2.2. Finally, using Eqs. (4) and (7) we find the local value of the azimuthal tension  $\sigma_\varphi$ :

$$\sigma_\varphi(z) = \frac{p_0 - \varepsilon g z \Delta\rho - \kappa_s(z) \sigma_s(z)}{\kappa_\varphi(z)} \quad (16)$$

In this way, the local values of the two surface tensions,  $\sigma_s(z)$  and  $\sigma_\varphi(z)$ , can be determined throughout the whole meniscus directly from the experimental data by using the force balance equations [27]. No model assumptions regarding the rheological behavior of the interfacial layer have been used.

## 2.2. Computational procedure of the capillary meniscus dynamometry (CMD)

Here, we describe the principle of the computational procedure of CMD [27], which is rather different from that of the conventional drop shape analysis (DSA) [26].

DSA is applicable to isotropic interfaces:  $\sigma_s = \sigma_\varphi = \sigma = \text{const}$ . The digitized drop/bubble profile is fitted to the Laplace equation of capillarity and two quantities,  $\sigma$  and  $p_0$ , are determined as adjustable parameters. The digitized profile typically contains 2–3 thousand points corresponding to pixels, from which only two constant parameters,  $\sigma$  and  $p_0$ , are determined by using the DSA procedure. In fact, the digitized meniscus profile contains much more information, which is utilized by the CMD procedure to determine the functions  $\sigma_s(z)$  and  $\sigma_\varphi(z)$  in each point of an anisotropic interface, as explained below.

First, the digitized meniscus profile is transformed from pixels to physical coordinates  $(r_k, z_k)$ . This includes (i) determination of the position of the symmetry axis, which does not necessarily coincide with the vertical axis of the experimental video frames; (ii) rotation of the profile to have the  $z$ -axis of the coordinate system directed along the axis of symmetry; (iii) calculation of the position of drop (bubble) apex or the position of the substrate (in the case of capillary bridge) in the new coordinate system; (iv) coordinate transformation that shifts the coordinate origin as shown in Fig. 1a and b. The illustrative  $r^2(z)$  plot in Fig. 2 is a result of this procedure applied to a capillary bridge formed by a bubble, which is bridging between a vertical capillary and a horizontal glass plate; see Section 5.

Next, the region of variation of  $z$  is divided to  $n$  equal parts: (20 parts in the illustrative Fig. 2, and at least 70 parts for the drops, bubbles and bridges in Sections 4–6):

$$z_{j-1} \leq z \leq z_j, \quad j = 1, \dots, n \quad (17)$$

Because of the small pixel size, each interval in Eq. (17) contains a large number of experimental  $(r_k, z_k)$  points, usually more than 30

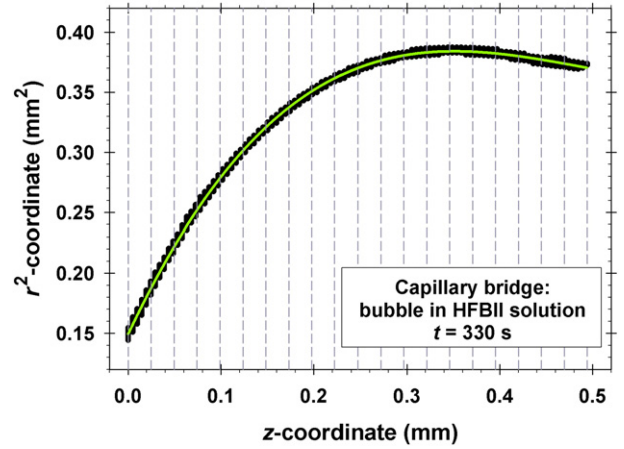


Fig. 2. Plot of  $r^2$ -vs.- $z$  for the experimental profile of a capillary bridge (the dots) formed by a bubble pressed against a substrate (Fig. 1b). The solid line represents the set of all interpolation curves according to Eq. (18) in all  $[z_{j-1}, z_j]$  intervals ( $j = 1, \dots, n$ ) confined between the neighboring vertical dashed lines.

points. In each of these small intervals, the experimental  $r^2(z)$  dependence is fitted with a second-order polynomial:

$$r^2 = a_j z^2 + b_j z + c_j \quad (z_{j-1} \leq z \leq z_j) \quad (18)$$

The coefficients  $a_j$ ,  $b_j$ , and  $c_j$  are determined as adjustable parameters by using the least squares method. The local value of the meniscus slope angle  $\theta$  is calculated from the expression:

$$\cot\theta = \frac{dr}{dz} = \frac{2a_j z + b_j}{2r} \quad (19)$$

Further, we calculate:

$$\sin\theta = (1 + \cot^2\theta)^{-1/2} = \left[1 + \left(\frac{2a_j z + b_j}{2r}\right)^2\right]^{-1/2} \quad (20)$$

$$\cos\theta = \pm(1 + \tan^2\theta)^{-1/2} = \frac{2a_j z + b_j}{[4r^2 + (2a_j z + b_j)^2]^{1/2}} \quad (21)$$

The meridional curvature is:

$$\kappa_s(z) = -\frac{d \cos\theta(z)}{dz} = \frac{2(b_j^2 - 4a_j c_j)}{[4r^2 + (2a_j z + b_j)^2]^{3/2}} \quad (22)$$

The middle point of each  $[z_{j-1}, z_j]$  interval is:

$$\zeta_j = \frac{z_{j-1} + z_j}{2}, \quad j = 1, \dots, n \quad (23)$$

The value  $I_j$  of the integral  $I$  in each  $[z_{j-1}, z_j]$  interval can be calculated from the recurrence formula (see Eq. (12)):

$$I_1 = \int_0^{\zeta_1} r^2(z) dz = \frac{1}{3} a_1 \zeta_1^3 + \frac{1}{2} b_1 \zeta_1^2 + c_1 \zeta_1 \quad (24)$$

$$I_j = \int_0^{\zeta_j} r^2(z) dz = I_{j-1} + a_j \frac{\zeta_j^3 - \zeta_{j-1}^3}{3} + b_j \frac{\zeta_j^2 - \zeta_{j-1}^2}{2} + c_1 (\zeta_j - \zeta_{j-1}) \quad (25)$$

$j = 2, 3, \dots, n$ . In view of Eq. (11), the value of the force  $F_p$  in the middle of each  $[z_{j-1}, z_j]$  interval is:

$$F_p(\zeta_j) \equiv \pi r^2(\zeta_j) \left( p_0 - \varepsilon g \zeta_j \Delta \rho \right) + \pi \varepsilon g \Delta \rho l_j \quad (26)$$

Next, Eqs. (14)–(16) are used to calculate  $\sigma_s(\zeta_j)$ ,  $\kappa_\phi(\zeta_j)$  and  $\sigma_\phi(\zeta_j)$  in the middle of each  $[z_{j-1}, z_j]$  interval using the values of the quantities  $r(\zeta_j)$ ,  $\sin\theta(\zeta_j)$ ,  $\kappa_s(\zeta_j)$  given, respectively, by Eqs. (18), (20) and (22) with  $z = \zeta_j$ . The pressure  $p_0$  in Eqs. (16) and (26) is supposed to be determined by pressure transducer measurements; see Section 3. In the case of capillary bridges, the constant  $F$  in Eq. (14) is determined from the fits of experimental data as explained in Section 5.

### 3. Experimental setups and materials

We carried out experiments with bubbles and drops attached to the tip of a glass or metal capillary of outer diameter 1.494 or 1.833 mm, respectively. In the case of buoyant bubbles and drops, a J-shaped capillary with attached pressure transducer was used (Fig. 3a). In the case of pendant drop, the drop is formed in the lower end of a vertical capillary (Fig. 3b). To determine  $p_0$  from the indications of the pressure transducer, the vertical distances  $h$  and  $H$  (Fig. 3) have been also measured; for details, see Ref. [27].

In our measurements, we utilized the setup for capillary pressure tensiometry (CPT) described in Ref. [42]. It is a DSA10 apparatus (Krüss GmbH, Hamburg, Germany) upgraded with a pressure transducer (model PX163-2.5BD5V), which registers the pressure inside the drop/bubble as a function of time. For a precise control of the bubble/drop volume, a piezo-driven membrane was used. Depending on the microscope magnification used in our experiments, we have one pixel equal to 12  $\mu\text{m}$  for larger objects (pendant drops and buoyant bubbles) and one pixel equal to 4.8  $\mu\text{m}$  for smaller objects (capillary bridges).

To obtain anisotropic (solidified) interfacial layers, we carried out experiments with buoyant bubbles in aqueous solutions of the protein hydrophobin HFBII (received from Unilever), which is a class II hydrophobin of molecular mass 7.2 kDa. It is composed from 70 amino acids with 4 disulfide bonds. HFBII is a relatively small and compact protein, which is stable upon heating up to 90 °C and upon adsorption on liquid and solid interfaces [48,49]. At the air/water and oil/water interfaces, HFBII forms rigid adsorption layers that exhibit high surface dilatational and shear elasticity [6–9,50–53].

As additive to HFBII, the nonionic surfactant Tween 20 ( $\text{C}_{58}\text{H}_{114}\text{O}_{26}$ –polyoxyethylene 20–sorbitan monolaurate, product of Sigma) was used;  $M_w = 1.228$  kDa; critical micelle concentration (CMC)  $\approx 50$   $\mu\text{M}$  [54]. As other additives, skim milk powder (SMP, received from Unilever) and NaCl (Merk) were used.

Another protein, used in our studies, was pea protein S85F provided by Unilever. This protein was dissolved in water at pH = 11 adjusted by

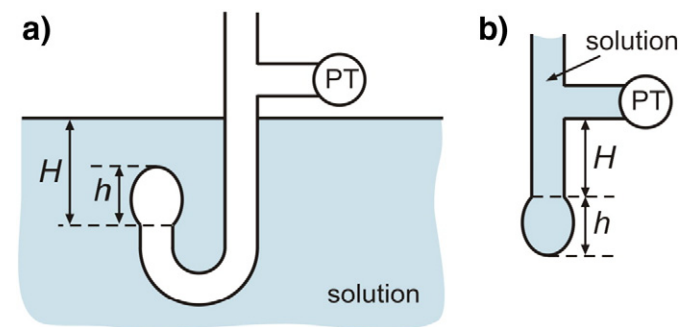


**Fig. 3.** Sketch of the experimental setups for measurements with (a) buoyant drops and bubbles and (b) pendant drops. The distances  $H$  and  $h$  have been measured to determine the capillary pressure at the apex,  $p_0$ , from the pressure difference measured by the pressure transducer (PT); see Ref. [27] for details.

the addition of NaOH. Subsequently, the pH was lowered to 6.4 with HCl. The obtained solutions were turbid. After centrifugation at 5000 $\times g$  for 30 min, the aqueous phase was clear and aggregates were not observed for a long period of time. The surface tension of the centrifuged and non-centrifuged solutions was the same. In our experiments with bridging bubbles we used centrifuged pea protein (PP) solutions and their mixtures with HFBII. The solutions with PP contain also 1 g/L  $\text{NaN}_3$  for antibacterial protection.

The used egg yolk was from food grade commercial chicken eggs. The working aqueous solutions contained 0.01 wt% egg yolk (EY). The actual concentration of surface active substances (proteins, phospholipids, etc.) is about twice lower, because the EY contains 48–50 % water [55].

Deionized water from Millipore Elix purification system (Millipore, USA) was used for preparation of all solutions. All experiments were carried out at temperature of  $25 \pm 1$  °C. In the experiments with bridging bubbles in protein solutions, the bubble and substrate have been equilibrated with the solution at least for 10 min before bringing them in contact. The dynamics of surface tension relaxation indicates that 10 min are enough to achieve equilibrium adsorption at the bubble surface for the working concentrations.

The used soybean oil (SBO) was a food grade commercial product from a local producer, which was purified by passing through a column filled with the adsorbents Florisil (Sigma–Aldrich, Germany) and Silica Gel 60. The purified SBO had interfacial tension of 31 mN/m against water. The difference between the densities of water and SBO was  $\Delta\rho = 0.078$  g/cm<sup>3</sup> at 25 °C. In the experiments with SBO drops in EY solutions, the drop and substrate have been equilibrated with the solution for 30 min before bringing them in contact. Longer equilibration time (as compared with that for bubbles) has been used because of the slower adsorption kinetics for the investigated specific emulsion systems. The equilibrium interfacial tension of SBO against 0.01 wt% aqueous solution of EY was 20.5 mN/m. In a part of the experiments with emulsion drops, glass plates hydrophobized with hexamethyldisilazane (HMDS) were used.

### 4. Application of CMD to bubbles and drops

#### 4.1. Interfaces with isotropic and anisotropic surface tension

It was demonstrated [27] that for bubbles and drops with isotropic surface tension (such as drops of pure water or bubbles in surfactant solutions) the CMD procedure yields exactly the same values of surface tension  $\sigma$  as the DSA and the Wilhelmy plate methods. In view of Eqs. (10) and (13), for an isotropic and uniform interface the plot of  $F_p$  vs.  $2\pi r \sin\theta$  should be a straight line of zero intercept and slope equal to  $\sigma$ . In Fig. 4a, this is illustrated for a bubble in a 0.005 wt% HFBII solution. As seen in this figure, initially the bubble surface tension is isotropic as indicated by the linear dependence of  $F_p$  vs.  $2\pi r \sin\theta$ . Both  $F_p$  and  $2\pi r \sin\theta$  have been calculated from the experimental bubble profile and the value of  $p_0$  using Eqs. (18), (19) and (26). Each point in Fig. 4a (and in all subsequent CMD plots) corresponds to the middle of a  $[z_{j-1}, z_j]$  interval; see Section 2.2 for details. The value  $\sigma = 60.8$  mN/m, determined from the slope of the straight line in Fig. 4a, is in agreement with Ref. [50], where it has been established that the HFBII adsorption layers are fluid for  $\sigma > 50$  mN/m, whereas they solidify for  $\sigma < 50$  mN/m.

In Fig. 4b, the deviation from linear dependence indicates that the surface of the same bubble (as in Fig. 4a) has solidified. The solidification was promoted by a small shrinkage of the bubble surface executed by the experimentalist by sucking of gas from the bubble, which has led to a decrease of the pressure  $p_0$  from 89.8 to 40.4 Pa. In Fig. 4b, a fit with linear regression is not applicable. Instead, one has to use the full CMD procedure and to calculate  $\sigma_s$  and  $\sigma_\phi$  as explained in the last paragraph of Section 2.2. In Fig. 5a, the obtained values of  $\sigma_s$  and  $\sigma_\phi$  are plotted vs. the vertical coordinate,  $z$ , with coordinate origin at the

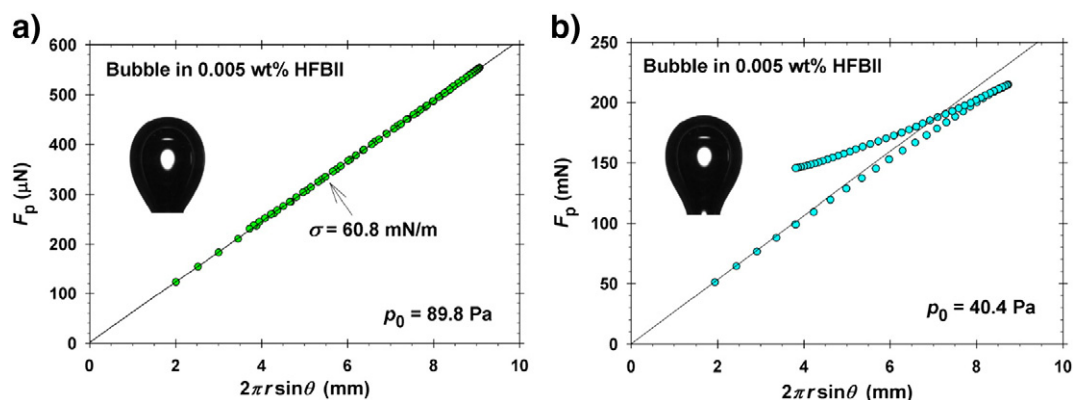


**Fig. 4.** Plot  $F_p$  vs.  $2\pi r \sin\theta$  for a bubble formed on the tip of a capillary in a 0.005 wt% HFBI solution. (a) The plot is linear, hence the adsorption layer is fluid; the slope yields  $\sigma = 60.8$  mN/m. (b) After the shrinkage of the bubble, the plot deviates from straight line (surface solidification);  $\sigma_s$  and  $\sigma_\phi$  have to be determined by the full CMD procedure [27].

bubble apex. One sees that  $\sigma_s$  and  $\sigma_\phi$  coincide only at the apex (the only point with isotropic curvature on the bubble profile), whereas for  $z > 0$  the azimuthal tension  $\sigma_\phi$  is systematically lower than  $\sigma_s$ , both of them being lower than the value 60.8 mN/m in Fig. 4a.

As seen in Fig. 5b, a subsequent shrinkage of the bubble surface, corresponding to a drop of  $p_0$  from 40.4 Pa to 21.1 Pa, has led not only to a greater surface anisotropy, but also to negative values of  $\sigma_\phi$  in the central zone of the bubble surface, where meridional wrinkles are observed. This result is in agreement with the theoretical study on wrinkling upon unidirectional compression of elastic interfacial layers [56], where it has been established that wrinkles appear at negative values of the surface tension component that is acting in direction perpendicular to the wrinkles (in our case –  $\sigma_\phi$ ).

A solidified interfacial layer (a membrane possessing shear elasticity) may have either positive or negative tension when it is subjected, respectively, to stretching or compression, just like an elastic spring. The tension-free state (of zero tension) is in the middle between the aforementioned two regimes [11]. The membrane possesses an additional degree of freedom – to bend. In the region of negative tension, it is energetically more favorable the membrane to bend instead of to decrease its area upon compression [56,57]. This is the reason for the appearance of wrinkles. In the case of HFBI, it was established that the wrinkling occurs at a critical packing fraction of protein molecules on the surface [58].

The determined values of  $\sigma_s$  and  $\sigma_\phi$  in the zone with wrinkles (Fig. 5b) represent average values of these two parameters. Indeed, the “microscopic” values of  $\sigma_s$  and  $\sigma_\phi$  in this zone oscillate around their mean values as functions of the azimuthal angle  $\phi$ .

In summary, the results demonstrate that the CMD method enables one to determine the surface tensions in the cases of both isotropic (Fig. 4a) and anisotropic (Fig. 5a,b) interfaces, including the cases with surface wrinkles [27].

#### 4.2. CMD vs. the drop shape analysis (DSA)

The DSA method is applicable to drops and bubbles with uniform and isotropic surface tension,  $\sigma$ . The bubble/drop profile is fitted with the Laplace equation of capillarity and two adjustable parameters,  $p_0$  and  $\sigma$ , which are determined from the fit [26]. An advantage of the DSA method is that it needs only a single set of data – that from the digitized drop profile (measurements of  $p_0$  are not necessary). However, the DSA method is inapplicable to interfacial layers with anisotropic stresses, like those in Fig. 5.

The CMD method (Section 2.2) has been developed to determine the stresses acting in anisotropic interfacial layers. In addition to the digitized bubble/drop profile, the CMD needs also measurements of the capillary pressure  $p_0$ . The principle of the computational procedure of CMD is rather different from that of DSA. No physical parameters are adjusted in CMD. The drop/bubble profile is divided to  $n$  small domains (Fig. 2) and in each of them the meniscus shape is fitted with a second order curve in accordance with Eq. (18). Then,  $F_p$  is determined from Eq. (26), and subsequently, the two independent surface stress balance equations are used to determine the meridional and azimuthal surface tensions  $\sigma_s$  and  $\sigma_\phi$  locally, in each point of the interface; see Eqs. (14), (16) and Fig. 5.

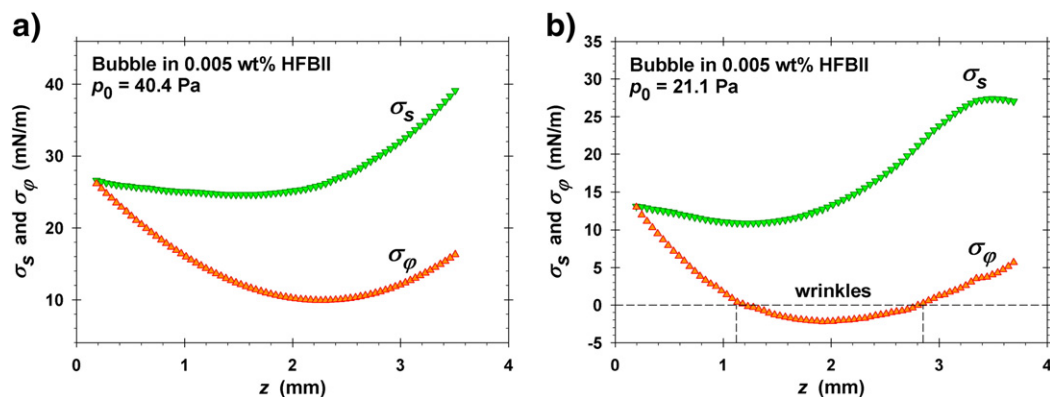


**Fig. 5.** Plots of the two components of surface tension,  $\sigma_s$  and  $\sigma_\phi$ , vs. the  $z$ -coordinate for bubble profiles with *anisotropic* surface tension;  $z = 0$  at the bubble apex. (a) The two surface tensions for the bubble profile in Fig. 4b with  $p_0 = 40.4$  Pa. (b) Subsequent sucking of gas leads to bubble shrinkage; the capillary pressure becomes  $p_0 = 21.1$  Pa; in the zone with  $\sigma_\phi < 0$ , meridional wrinkles are observed on the bubble surface [27].

A solidified nonspherical interfacial layer (e.g. a protein adsorption layer on the surface of a pendant drop or buoyant bubble) with anisotropic surface tension does not obey the conventional Laplace equation of capillarity. For this reason, the error of the Laplace fit determined by the DSA apparatus increases, which can be considered as an indication for surface solidification [50]. However, the CMD method is more sensitive to the surface solidification than the error of the DSA Laplace fit, as demonstrated in Fig. 6.

Fig. 6 shows the variation of surface tension with time  $t$  for a pendant drop from an aqueous solution of 0.001 wt% HFBII. In this figure,  $\sigma_{\text{DSA}}$  is the surface tension given by the DSA apparatus; the error of the Laplace fit given by this apparatus is also plotted;  $\sigma_{\text{CMD}}(0) = \sigma_s = \sigma_\varphi$  is the surface tension at the drop apex measured by CMD.

For  $t < 450$  s, the data in Fig. 6 indicate that  $\sigma_{\text{DSA}} = \sigma_{\text{CMD}}(0)$ , which means that the interfacial layer is isotropic. For  $t > 450$  s,  $\sigma_{\text{CMD}}(0)$  exhibits a minimum, a maximum and a second minimum, which are due to a consecutive compression, expansion and second compression of the drop surface executed by the experimentalist. Wrinkles appear on the drop surface upon compression; see the photo in Fig. 6. The upper curve in this figure shows that  $\sigma_{\text{DSA}}$  varies very little for  $t > 450$  s, i.e. the DSA is insensitive to the interfacial compressions and expansions ( $\sigma_{\text{DSA}}$  is almost constant,  $\approx 50$  mN/m, in this region). Indications for surface solidification are given by the error of the Laplace fit, which exhibits local maxima in the regions with the greatest compressions. However, the most sensitive indicator for surface solidification is the difference between  $\sigma_{\text{DSA}}$  and  $\sigma_{\text{CMD}}(0)$ . Indeed, as seen in Fig. 6 this difference becomes noticeable at  $\sigma \approx 60$  mN/m, whereas the Laplace fit error indicates the onset of anisotropy markedly later, at  $\sigma \approx 50$  mN/m, as in Ref. [50].

The difference between  $\sigma_{\text{DSA}}$  and  $\sigma_{\text{CMD}}(0)$  can be considerable. Thus, at  $t = 900$  s,  $\sigma_{\text{DSA}} = 55.3$  mN/m, whereas  $\sigma_{\text{CMD}}(0) = 14.7$ , with a difference of 40.6 mN/m between them (Fig. 6). The reason for this difference is related to the fact that DSA uses both  $\sigma$  and  $p_0$  as adjustable parameters. The computer program of DSA is minimizing the difference between the calculated Laplace profile and the non-Laplacian real profile of the solidified drop/bubble, which leads to obtaining of non-physical values of  $\sigma$  and  $p_0$  by DSA; see Ref. [27], Table 1 therein.

The numerical procedure of CMD is fast and it has a fixed duration, so that the method can be automated and applied to determine the dynamics of variation of  $\sigma_s$  and  $\sigma_\varphi$  in real time, during a given process. This could be used for the creation of feedback that keeps the bubble surface area constant during the experiment. In contrast, the duration of the numerical procedure of DSA depends on the degree of drop/bubble deformation, which affects the duration of the numerical minimization used to determine the adjustable parameters  $p_0$  and  $\sigma$ . It should be noted that the CMD is applicable even at small gravitational

deformations, e.g. to determine the interfacial tension of the boundary between two liquids of very close mass densities. (An example is given in Section 6.3 for the water/soybean oil boundary, for which the density difference is  $\Delta\rho = 0.078$  g/cm<sup>3</sup>.)

The CMD procedure is applicable also to fluid interfaces to determine the single isotropic surface tension,  $\sigma$ , which is constant along the interface. In this simpler case, it is not necessary to measure independently  $p_0$ . Instead,  $p_0$  can be determined simultaneously with  $\sigma$ , as a second adjustable parameter (as with the DSA). In this case the advantage of CMD is that the meniscus profile is fitted with an algebraic equation that is linear with respect to  $\sigma$  and  $p_0$ , see Eq. (30) in Ref. [27]. Thus, these two adjustable parameters can be determined with a single computation, without using any minimization procedure with multiple iterations.

#### 4.3. Comparison of CMD with other theoretical approaches to anisotropic interfaces

As demonstrated above, the CMD allows one to directly determine the two surface tensions,  $\sigma_s$  and  $\sigma_\varphi$ , in every point of the bubble/drop profile and in each moment of time,  $t$ . The alternative elastic-plate approach [21–25] assumes that a given model from theory of elasticity can be applied to fit the drop/bubble profile. The constants of this model (e.g. Young modulus and Poisson ratio) are determined as adjustable parameters from the best fit. Next, the two surface tensions,  $\sigma_s$  and  $\sigma_\varphi$ , are calculated using the respective expressions of the used model. The problems encountered by the elastic-plate approach have been discussed in details in Ref. [27]. Here, a brief summary of the main points is given:

- (i) It is not sure whether the interfacial layer does really obey the presumed purely elastic model. For example, protein adsorption layers have been found to obey different viscoelastic thixotropic models [2,52,53]. The CMD could help for model discrimination – different rheological models could be tested against the CMD data for  $\sigma_s$  and  $\sigma_\varphi$ , not only against data for the bubble/drop profile.
- (ii) In the elastic-plate approach, a reference state with isotropic stresses and zero (by definition) strain is needed to quantify the strains and stresses upon subsequent deformations. However, the initial isotropic state is not *a priori* known, but it can be determined by CMD (see Fig. 6).
- (iii) The theory of elastic plates and shells implicitly presumes a closed system, i.e. the lack of exchange of molecules between the interfacial layer and the bulk. This assumption is not fulfilled for a system with adsorption dynamics. In contrast, the CMD method proposed in the present article is applicable to both closed and open systems, just like the DSA for isotropic interfaces.

In conclusion, a complete theoretical description of the behavior of an anisotropic interfacial layer, including the dependences of  $\sigma_s$  and  $\sigma_\varphi$  on the spatial coordinates and time, always demands the use of a certain rheological model. In this respect, the determination of  $\sigma_s$  and  $\sigma_\varphi$  by CMD can be considered as a preliminary step that serves as a base for formulation of an adequate rheological model.

#### 5. Capillary bridge dynamometry (CBD)

The adhesion of bubbles and drops to solid surfaces has been studied in relation to the interaction of foams and emulsions with the walls of containers. The adhesion force can be investigated by experiments with bubbles/drops, which are formed at the tip of a capillary and after that pressed against a horizontal solid substrate; see Fig. 7. In such experiments, the bubble/drop forms an axisymmetric capillary bridge between the capillary and the substrate. Analyzing the bridge profile, one can determine the surface tension of the bridge and the

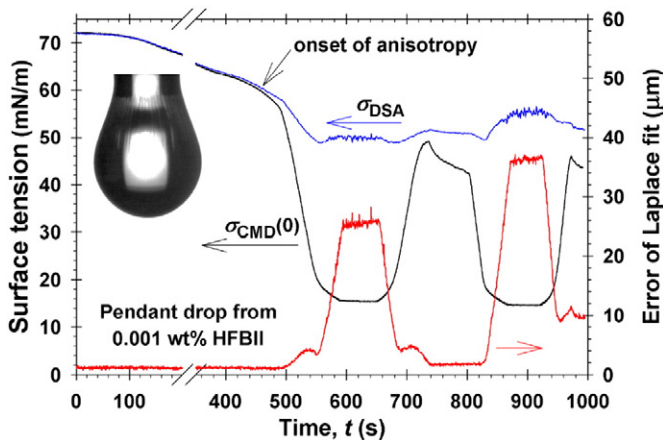
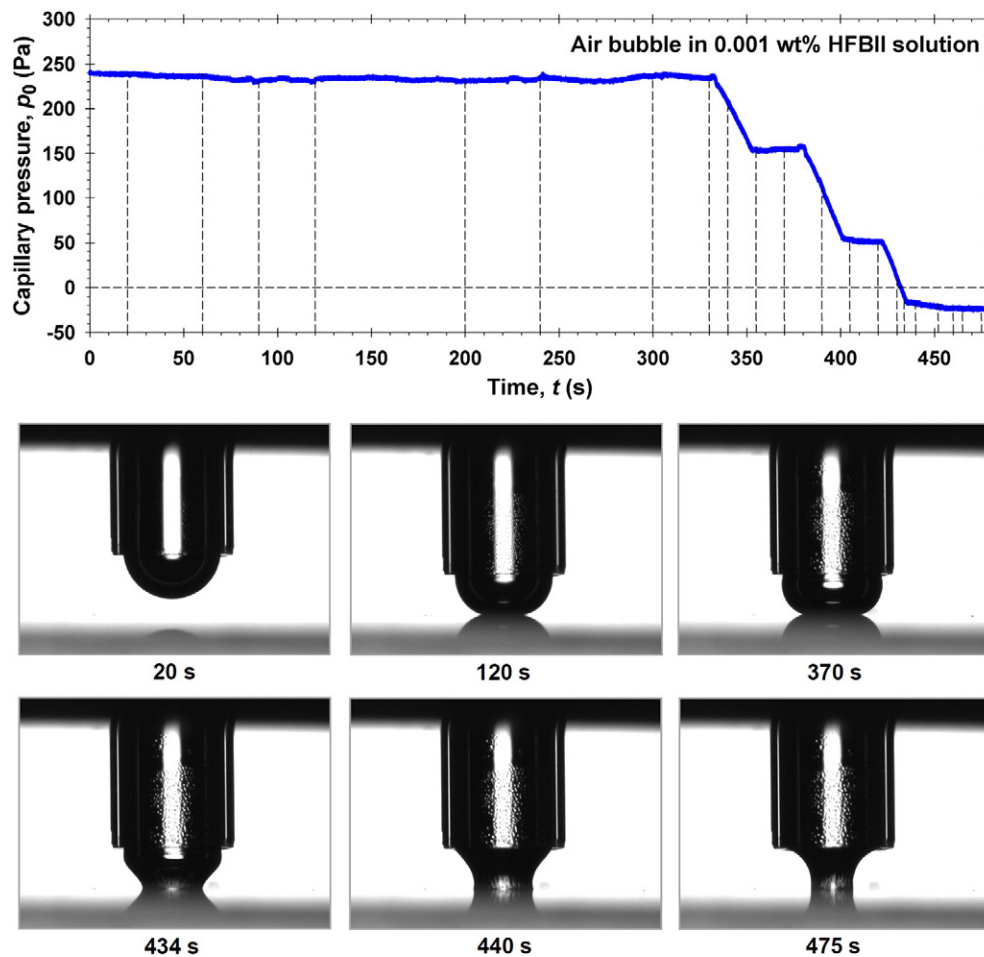


Fig. 6. Time dependencies of the surface tension  $\sigma_{\text{DSA}}$  and the error of the Laplace fit given by the DSA apparatus, as well as of the surface tension at the drop apex,  $\sigma_{\text{CMD}}(0)$ , measured by CMD. The data are for a pendant drop from 0.001 wt% HFBII solution [27].



**Fig. 7.** Plot of experimental data for the capillary pressure  $p_0$  vs. time  $t$  for an air bubble bridging between a capillary and a glass substrate in 0.001 wt% HFBII solution. The vertical dashed lines correspond to moments of time, at which video frames have been processed; six of them are shown in the figure. From the digitized profiles, the surface tension and the capillary bridge force,  $F$ , have been determined (see the text).

capillary-bridge force,  $F$ , which is related to the force of bubble/drop adhesion to the substrate. Such analysis has been already done by assuming that a neo-Hookean model of elastic plates is obeyed by the interfacial layer [24].

Here, we demonstrate that the method of capillary meniscus dynamometry is applicable also to capillary bridges without presuming any interfacial rheological model. The theoretical basis is the same as in Section 2.2, with  $F \neq 0$ . Depending on whether the surface tension of the capillary bridge is isotropic, partially isotropic, or anisotropic, three different approaches to the determination of  $F$  by data processing can be applied, as described below. Because of its specificity, this methodology will be termed *capillary bridge dynamometry* (CBD).

An example for CBD experiment is shown in Fig. 7 for a bubble formed at the tip of a vertical capillary in an aqueous solution of 0.001 wt% HFBII. Before its contact with the substrate, the bubble surface was equilibrated for 10 min with the solution until its surface tension levels off (at a value  $\sigma = 62.5$  mN/m). The bubble volume was varied by pumping or sucking of air through the capillary. This was carried out with the help of a piezoelectric membrane, which provides a fine control of the bubble volume and its contact area with the substrate. During the whole experiment, the distance between the capillary and the glass substrate was constant.

First, by supplying of gas to the bubble, its size is increased. At  $120 \leq t \leq 300$  s, the lower part of the bubble is pressed against the horizontal glass plate. After that, at  $300 < t < 478$  s the volume of gas in the bubble is decreased until the bubble detaches from the substrate. The variation of the pressure difference detected by the transducer is

shown in Fig. 7. To detach the bubble, the pressure was decreased in three steps of about 80 Pa each. In this experiment, 22 video frames of the bubble profile (six of them shown in Fig. 7) were processed. From the digitized profiles, the surface tension and the capillary bridge force,  $F$ , have been determined as explained below.

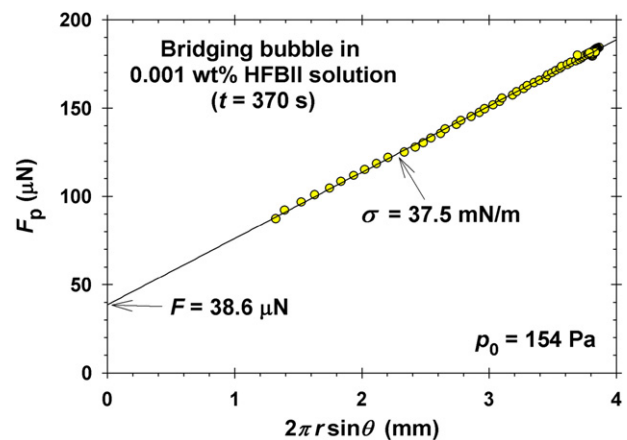


**Fig. 8.** Plot of  $F_p$  vs.  $2\pi r \sin\theta$  in accordance with Eq. (13) for a bridging bubble at  $t = 370$  s; see Fig. 7. The slope yields surface tension  $\sigma = 37.5$  mN/m, whereas the intercept gives capillary-bridge force  $F = 38.6$   $\mu$ N.

### 5.1. Bridge with isotropic surface tension

In Fig. 8, the plot of  $F_p$  vs.  $2\pi r \sin\theta$  is linear. In accordance with Eq. (13), this indicates that the surface tension is isotropic ( $\sigma_s = \sigma_\varphi = \sigma$ ) and constant throughout the whole surface of the capillary bridge. For the experiment illustrated in Fig. 7, the processed bubble profiles indicate that the surface tension is isotropic for  $120 \leq t \leq 430$  s. For the example in Fig. 8 ( $t = 370$  s), the slope of the linear regression yields  $\sigma = 37.5$  mN/m, whereas from the intercept we determine  $F = 38.6$   $\mu$ N. In view of the definition, Eq. (9),  $F > 0$  ( $F < 0$ ) corresponds to repulsive (attractive) capillary-bridge force between the capillary and substrate. According to the Plateau classification of the capillary bridges,  $F > 0$  can be realized only with convex capillary bridges of nodoid generatrix [47]. (In our case, the nodoid is slightly deformed due to the effect of gravity.)

In general, the plots in Fig. 4a (buoyant bubble) and Fig. 8 (bridging bubble) are very similar, with the only difference that in the former case  $F = 0$  (no intercept), whereas in the latter case  $F > 0$ . In both cases, the procedure from Section 2.2 was applied to process the experimental data and to determine  $F_p$ ,  $r$  and  $\theta$ . Each point in Figs. 4 and 8 corresponds to the values of these parameters in the middle of a  $[z_j, z_{j-1}]$  interval.

### 5.2. Bridge with anisotropic surface tension and wrinkles

For the bridging bubble in Fig. 7, at  $434 \leq t \leq 478$  s the hydrophobic interfacial layer solidifies and meridional wrinkles appear. The surface tension is anisotropic and the plot of  $F_p$  vs.  $2\pi r \sin\theta$  is no longer linear (as it was for the isotropic surface in Fig. 8). In the case of capillary bridge with wrinkles, another linear data plot is possible, as follows.

In the zone with wrinkles, the azimuthal surface tension is expected to take very low values [25,56,57], i.e.  $\sigma_\varphi \approx 0$ . Then, from the tangential stress balance, Eq. (3), we obtain:

$$\frac{d}{dr}(r\sigma_s) = \sigma_\varphi \approx 0 \Rightarrow (r\sigma_s) = \text{const.} \quad (27)$$

In such a case, Eq. (13) implies that the plot of  $F_p$  vs.  $\sin\theta$  should be a straight line with slope  $2\pi(r\sigma_s)$  and intercept  $F$ .

As before,  $F_p$  and  $\theta$  are determined from the meniscus profile and the value of  $p_0$  measured by pressure transducer (see Section 2.2). For all processed video frames in the region of solidified adsorption layer,  $434 \leq t \leq 478$  s, the plot of  $F_p$  vs.  $\sin\theta$  complies very well with a straight line in the zone with wrinkles, which confirms the validity of the assumption  $\sigma_\varphi \approx 0$ . This is illustrated in Fig. 9a for the bridge that corresponds to  $t = 475$  s. The constant parameter  $F$  (the capillary-bridge force) is determined from the intercept of the linear regression. The obtained negative value,  $F = -22$   $\mu$ N, means that the capillary-bridge force is attractive in this case. Fig. 9b shows  $\sigma_s$ , which is calculated from Eq. (14) with the determined value of  $F$ .

All processed video frames from the process of bubble attachment and detachment (Fig. 7) belong either to the case of isotropic surface (Section 5.1) or anisotropic surface with wrinkles (the present section). Correspondingly, the capillary bridge force,  $F$ , was determined from linear plots like those in Figs. 8 and 9a. All obtained values of  $F$  are shown in Fig. 9c. Initially (for  $t \leq 300$  s),  $F$  increases with time, which corresponds to pressing of the bubble to the substrate by pumping of gas in it ( $p_0$  increases). After that,  $F$  (and  $p_0$ ) decreases with time due to sucking of gas from the bubble. Eventually,  $F$  changes sign and becomes negative (attractive). At these final stages of bubble detachment,  $p_0$  is also negative. The relation between the measured capillary-bridge force,  $F$ , and the force of bubble adhesion to the substrate is considered in Section 6.

### 5.3. Bridge with partially isotropic surface tension

In principle, it is possible to have an intermediate case between those considered in Sections 5.1 and 5.2, viz. a part of the bridge surface

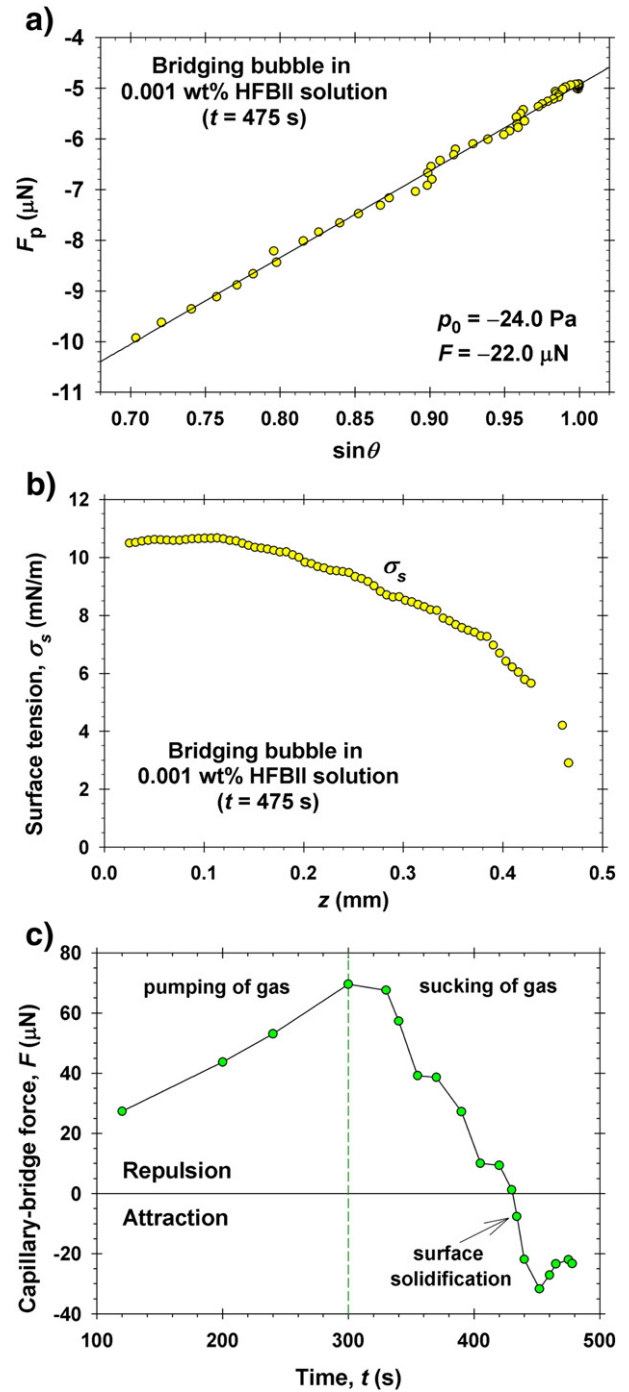
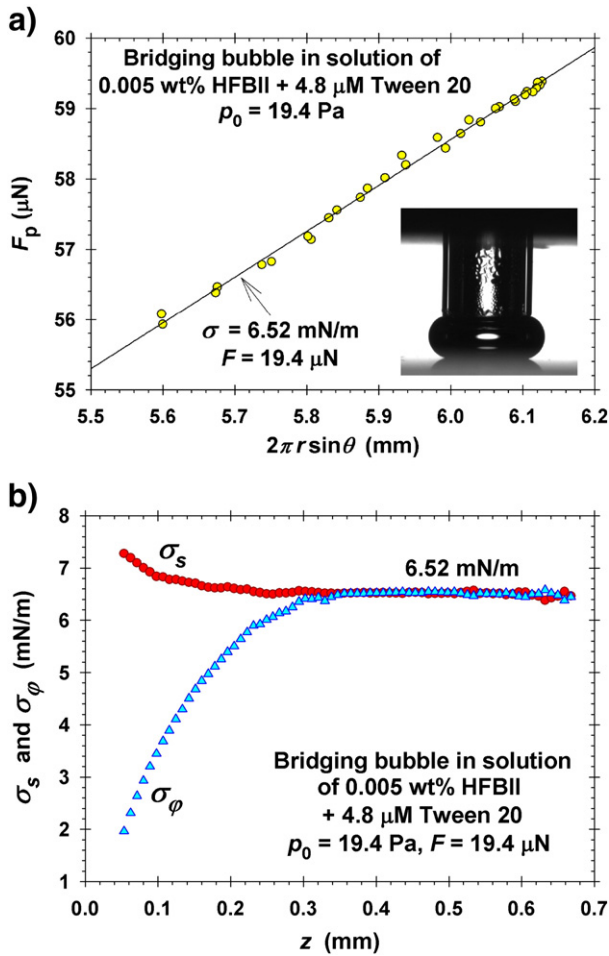


Fig. 9. (a) Plot of  $F_p$  vs.  $\sin\theta$  in accordance with Eqs. (13) and (27) for a bridging bubble at  $t = 475$  s; see Fig. 7. (b) Plot of the “meridional” surface tension  $\sigma_s$  vs. the vertical coordinate  $z$ , calculated from Eq. (14). (c) Plot of the capillary-bridge force  $F$  vs. time  $t$  for the considered bridging bubble.

might have isotropic tension, whereas the rest of the surface – anisotropic tension. This relatively rare intermediate case was not observed in the experiments with bubbles in 0.001 wt% HFBII (Fig. 7), but it was observed in experiments with bubbles in a solution of 0.005 wt% HFBII with  $4.8$   $\mu$ M added Tween 20; see Fig. 10. The points from the upper part of the digitized bridge profile obey a linear dependence when plotted as  $F_p$  vs.  $2\pi r \sin\theta$  (Fig. 10a), i.e. the surface tension in this part of the bridge is isotropic ( $\sigma_s = \sigma_\varphi = \sigma$ ). The slope of the linear plot yields  $F = 19.4$   $\mu$ N. Because  $F$  is constant along the whole bridge profile, the same value of  $F$  can be used also for the lower, solidified part of the bridge surface. Then,  $\sigma_s$  and  $\sigma_\varphi$  can be calculated from Eqs. (14) and (16). The



**Fig. 10.** Application of CBD to a bubble interacting with a glass plate in a solution of 0.005 wt% HFBII and 4.8  $\mu\text{M}$  Tween 20. (a) Plot of  $F_p$  vs.  $2\pi r \sin\theta$  in accordance with Eq. (13) indicating isotropic surface tension  $\sigma$  in the upper part of the bubble. (b) Plots of  $\sigma_s$  and  $\sigma_\phi$  vs.  $z$  indicating solidification of the meniscus near  $z = 0$  (near the glass plate), where  $\sigma_s \neq \sigma_\phi$ .

results are shown in Fig. 10b. One sees that in the lower part of the capillary bridge (for  $z < 0.3$  mm)  $\sigma_s$  slightly increases, whereas  $\sigma_\phi$  strongly decreases when approaching the substrate (when decreasing  $z$ ). (This video frame is just before the appearance of wrinkles, which happens at  $\sigma_\phi \rightarrow 0$ .) In contrast, in the upper part of the bridge, the surface tension is isotropic,  $\sigma_s = \sigma_\phi = 6.5$  mN/m, in agreement with Fig. 10a.

## 6. Adhesion force determination from CBD data

### 6.1. Mechanical balances in the adhesion zone of a bubble or drop

The capillary-bridge force  $F$  characterizes the interaction between the capillary and the substrate mediated by the bridging bubble or drop (Fig. 7). To identify the parameter that characterizes the adhesion force, we have to consider the balance of forces in the flat thin liquid film formed in the zone of contact of the bubble/drop with the substrate; see Fig. 11a. The upper surface of this film is the bubble/drop surface, whereas the lower film surface is the solid substrate. It is assumed that the film is plane-parallel for  $r \leq r_c$ . The interactions in the contact zone are described by the phenomenological theory of the thin liquid films [59–61].

First, let us consider the force balance per unit area of the upper film surface. In general, the pressure  $p_2$  inside the bubble (or drop) is different from the outer pressure,  $p_1$ , because of the capillary pressure of the meniscus:  $p_0 = p_2 - p_1$ . Per unit area of the upper film surface, the inner pressure  $p_2$  is counterbalanced by the sum of the outer pressure  $p_1$  and

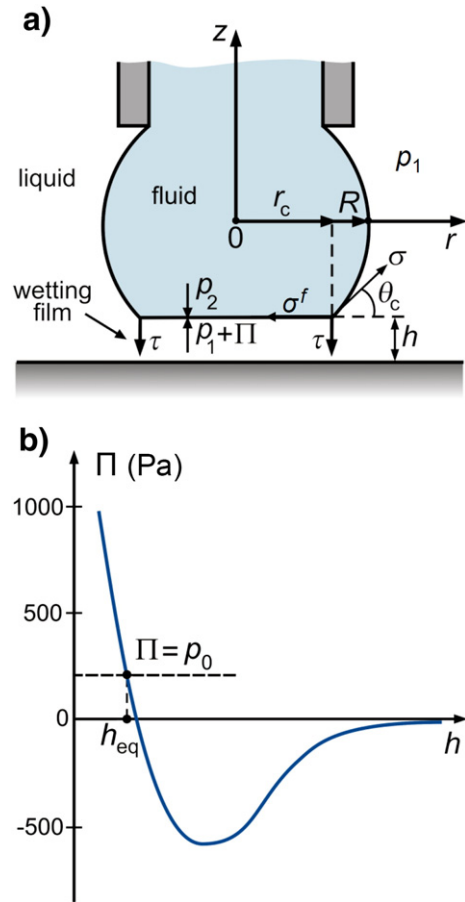


**Fig. 11.** (a) Force balances for a fluid particle (bubble, drop) adherent to a solid substrate;  $h$  is the thickness of the wetting film intervening between the particle and substrate;  $p_1$  and  $p_2$  are the pressures outside and inside the particle;  $\Pi$  is the disjoining pressure of the film;  $\sigma$  and  $\sigma^f$  are the surface tensions of the meniscus and of the film surface;  $\tau$  is the transversal tension;  $r_c$  and  $\theta_c$  are the contact radius and angle. (b) A typical  $\Pi$  vs.  $h$  dependence;  $h_{eq}$  is the equilibrium film thickness, which corresponds to  $\Pi = p_0$ ; see Eq. (28).

the disjoining pressure  $\Pi$  (see Fig. 11a):  $p_2 = p_1 + \Pi$ . Then, for an equilibrium film the disjoining pressure is equal to the capillary pressure [59]:

$$\Pi = p_0 = p_2 - p_1 \quad (28)$$

The disjoining pressure  $\Pi$  accounts for the interaction between the two film surfaces. The  $\Pi(h)$  dependence is a superposition of repulsive surface forces (electrostatic, hydration, steric) and attractive surface forces (van der Waals, hydrophobic, bridging by macromolecules, etc.) [47,62–64]. Positive (negative)  $\Pi$  corresponds to repulsion (attraction) between the two film surfaces. A typical dependence of  $\Pi$  on the film thickness,  $h$ , is presented in Fig. 11b. At smaller  $h$  values, the repulsive forces prevail in the film ( $\Pi > 0$ ). Stable is the branch of the  $\Pi(h)$  dependence, for which  $\Pi$  increases with the decrease of  $h$ , that is  $d\Pi/dh < 0$  [63]. The intersection point of the horizontal line  $\Pi = p_0$  with the stable branch of the  $\Pi(h)$  curve determines the equilibrium film thickness,  $h_{eq}$ ; see Eq. (28) and Fig. 11b. Note that equilibrium thickness may exist even at negative  $p_0$ .

Second, let us consider the force balance per unit length of the contact line (of radius  $r_c$ ) at the periphery of the upper film surface (Fig. 11a). The tangential and normal projections of this force balance (with respect to the film surface) read [60,61]:

$$\sigma^f = \sigma \cos\theta_c \quad (\text{tangential balance}) \quad (29)$$

$$\tau = \sigma \sin \theta_c \quad (\text{normal balance}) \quad (30)$$

Here,  $\sigma$  is the meniscus surface tension (for anisotropic surfaces,  $\sigma$  is to be replaced by the value,  $\sigma_c$ , of the “meridional” surface tension  $\sigma_s$  at the contact line);  $\sigma^f$  is the surface tension of the upper film surface;  $\theta_c$  is the contact angle;  $\tau$  is the *transversal tension*, which accounts for the excess attraction between the two film surfaces in the region of the contact line. The latter quantity can be expressed in the form [61]:

$$\tau = \frac{1}{r_c} \int_0^R [\Pi^{\text{id}} - \Pi(r)] r dr \quad (31)$$

$\Pi^{\text{id}}$  is the disjoining pressure in the idealized system (viz.  $\Pi^{\text{id}} = p_0 = \text{const.}$  inside the film, and  $\Pi^{\text{id}} = 0$  outside the film), whereas  $\Pi(r)$  is the variable disjoining pressure across the narrow transition zone between the film and the meniscus.

Eq. (30) means that the excess adhesive forces at the contact line, expressed by  $\tau$ , counterbalance the normal projection of the meniscus surface tension,  $\sigma \sin \theta_c$ . These adhesive forces could be either long-ranged, like the van der Waals force, or short range, like the hydrophobic force [64] and the attraction due to extension of macromolecules (e.g. proteins), which are bridging between the two film surfaces.

The total balance of forces acting on the fluid particle (bubble, drop) in Fig. 11a reads [47,65,66]:

$$F_{\text{ext}} = 2\pi r_c \tau - \pi r_c^2 \Pi \quad (32)$$

In other words, the external force,  $F_{\text{ext}}$ , acting along the normal to the substrate, is counterbalanced by the action of  $\tau$  along the whole contact line of length  $2\pi r_c$  minus the force due to disjoining pressure  $\Pi$  multiplied the area of the upper film surface,  $\pi r_c^2$ . In the case of capillary bridge,

$$F_{\text{ext}} = -F \quad (33)$$

where  $F$  is the capillary-bridge force. Note that in view of Eqs. (28), (30) and (33), Eq. (32) is equivalent to Eq. (9). If there is no external force,  $F_{\text{ext}} = 0$ , the bubble or drop can remain attached to the substrate (as often observed) if the two terms in the right hand side of Eq. (32) counterbalance each other,  $2\pi r_c \tau = \pi r_c^2 \Pi$ .

At equilibrium, the role of the repulsive disjoining pressure  $\Pi$  is to keep the film thickness uniform, whereas in view of Eq. (32) the role of the attractive transversal tension  $\tau$  is to keep the bubble (drop) attached to the surface. In other words, the bubble (drop) sticks to the surface with its periphery (contact line), where the attractive forces prevail, whereas repulsive forces prevail inside the film [47,65,66]. Hence, the adhesion is dominated by the effect of transversal tension,  $2\pi r_c \tau$ , in Eq. (32). As a rule, the effect of disjoining pressure,  $-\pi r_c^2 \Pi$ , opposes the adhesion. As an exception, the disjoining pressure force could be adhesive in the case of negative capillary pressure,  $\Pi = p_0 < 0$ , which can be realized for some concave capillary bridges (see e.g. Fig. 7).

## 6.2. Bubble adhesion to surfaces – data analysis

As already mentioned, in the experiments on bubble attachment/detachment we determine the capillary pressure,  $p_0$ , contact radius,  $r_c$ , and capillary-bridge force,  $F$ , as functions of time,  $t$ . Next, from Eq. (32), along with Eqs. (28) and (33), we can calculate the transversal tension:

$$\tau = \frac{\pi r_c^2 p_0 - F}{2\pi r_c} \quad (34)$$

In Fig. 12,  $\tau$  and  $r_c$  are plotted vs.  $t$  for solutions containing hydrophobin HFBII. Analogous results are plotted in Fig. 13a,b for solutions containing pea protein (PP). Finally, in Fig. 13c the surface tension

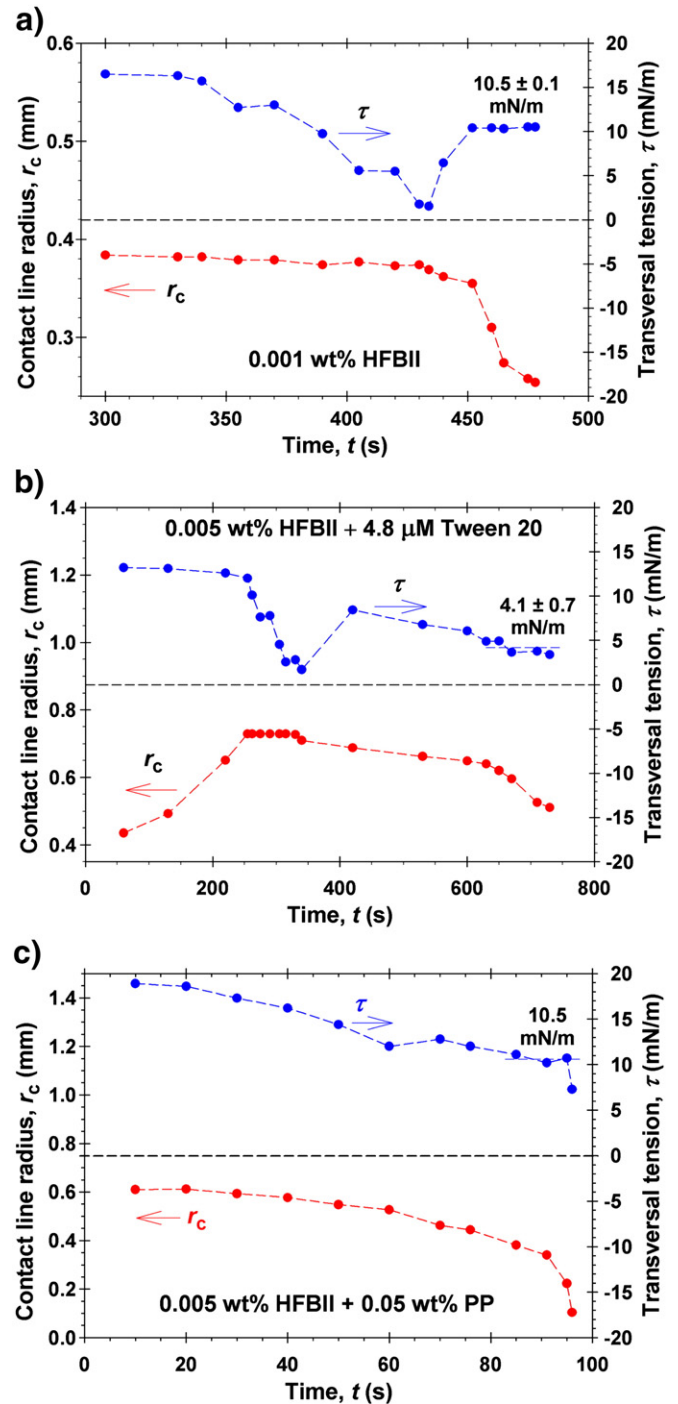


Fig. 12. Plots of the contact radius  $r_c$  and transversal tension  $\tau$  vs. time  $t$  for bridging bubbles in solutions of (a) 0.001 wt% HFBII; (b) 0.005 wt% HFBII + 4.8  $\mu\text{M}$  Tween 20; (c) 0.005 wt% HFBII + 0.05 wt% pea protein (PP).

$\sigma$  of the bridging bubble, determined by CBD, is also presented as a function of  $t$ . In the cases when the bridge surface solidifies, like those in Fig. 12a,b,  $\sigma$  is presented by  $\sigma_c$  – see Eq. (9). For all other systems, those with PP in Figs. 12c and 13a,b,  $\sigma$  is isotropic and uniform throughout the bridge surface.

In Fig. 12, for the systems with HFBII the variation of  $\tau$  during an experiment follows the variations of surface tension  $\sigma$ . This is understandable, because  $\tau$  should counterbalance the normal projection of surface tension,  $\sigma \sin \theta$ . Initially, the sucking of gas from the bubble leads to interfacial deformation at (almost) fixed contact line, but increasing contact angle  $\theta_c$ . At the last stages of the detachment process,  $r_c$  decreases

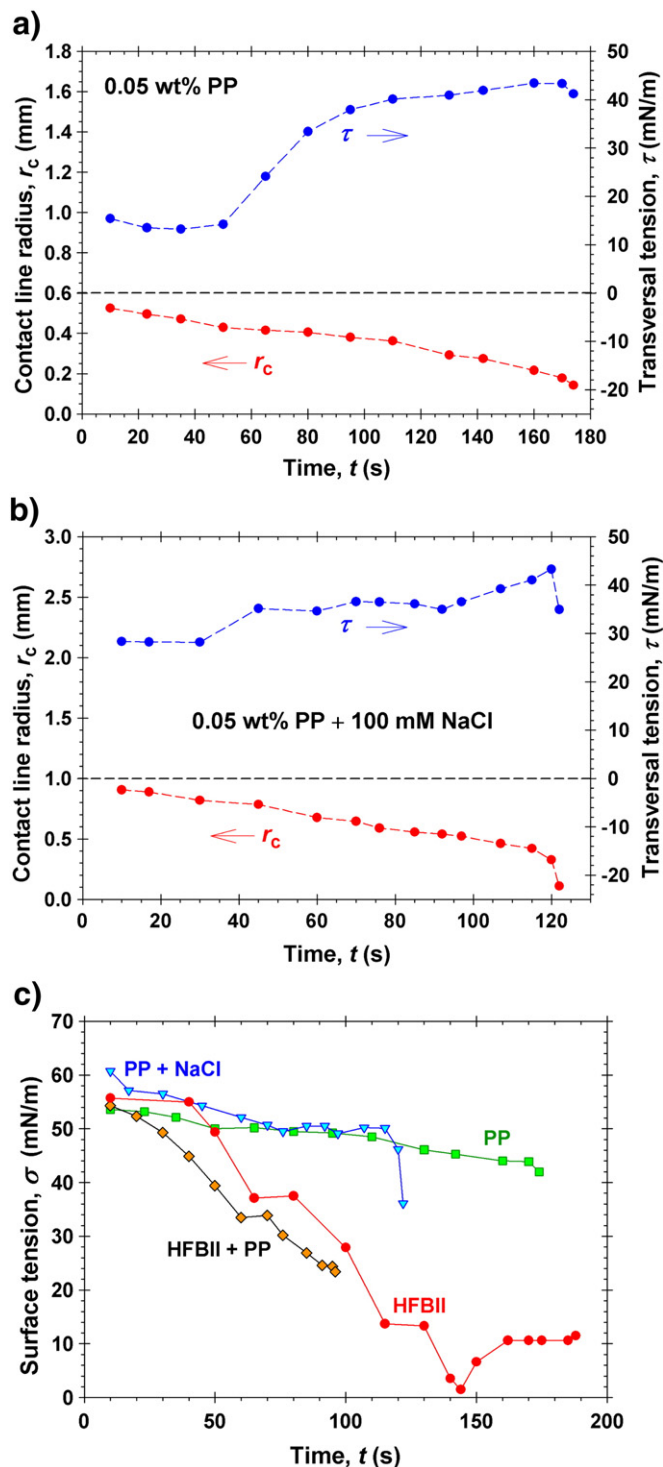


Fig. 13. Plots the contact radius  $r_c$  and the transversal tension  $\tau$  vs. time  $t$  for bridging bubbles in solutions of (a) 0.05 wt% pea protein (PP); (b) 0.05 wt% PP + 100 mM NaCl. (c) Comparison of the time variations of surface tension for the bubbles from Figs. 12a,c and 13a,b.

faster (shrinkage of the contact area), and  $\tau$  reaches an almost constant stationary value, which is about 10.5 mN/m for the systems in Fig. 12a and c. Constant stationary values of  $\tau$  have been established also for shrinking bubbles located below the surface of a surfactant solution [67,68].

In Fig. 13a and b, for the systems with PP and PP + NaCl the tendency is the opposite – the variation of  $\tau$  does not follow the variation of  $\sigma$ . The data show that  $\tau$  increases, whereas  $\sigma$  monotonically decreases in

the course of the experiment. This is related to a significant increase of the contact angle,  $\theta_c$ , which compensates the decrease of  $\sigma$ . (Note that in all considered experiments on bubble detachment,  $\theta_c$  is a dynamic, rather than equilibrium, contact angle.) The larger values of  $\tau$  indicate a stronger adhesion of the bubbles in the solutions of PP in comparison with those containing HFBII. Additional factor is the rigidity of the respective adsorption layers in relation to their behavior upon interfacial compression. The HFBII adsorption layers solidify and behave as elastic membranes, which form wrinkles upon compression [57,69]. The PP also irreversibly adsorbs at the air/water interface, but its adsorption layers have isotropic surface tension. Upon compression, they become thicker, i.e. multilayers (instead of wrinkles) are formed.

Our next task is to characterize quantitatively, with a given value of an appropriate parameter, the adhesion of bubbles and drops to substrates. In search of such parameter, in Fig. 14 we have plotted the three terms in Eq. (32) as function of  $t$  for six different experiments. Note that the external force,  $F_{\text{ext}}$ , is equal to the sum of the transversal tension term,  $2\pi r_c \tau$ , and the disjoining pressure term,  $-\pi r_c^2 \Pi$ . The decreasing branches of the curves  $-\pi r_c^2 \Pi$  vs.  $t$  correspond to pumping of gas in the bubble, whereas the increasing branches – to sucking of gas.

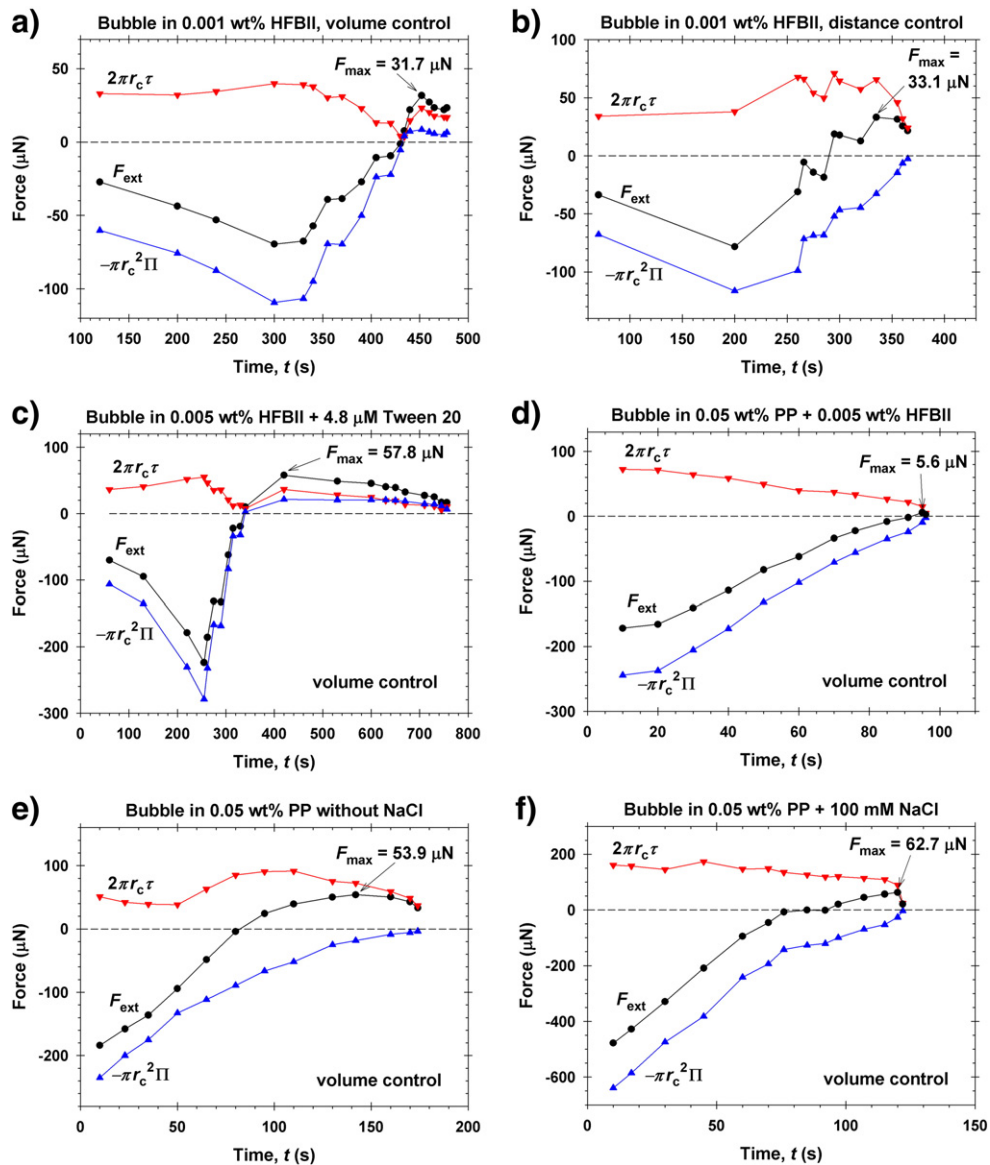
Positive values of  $F_{\text{ext}}$  mean that the external force (due to the capillary) is acting upwards and tends to detach the bubble from the substrate. It is remarkable that in all plots in Fig. 14,  $F_{\text{ext}}$  has a maximum value, which is denoted by  $F_{\text{max}}$ . Physically,  $F_{\text{max}}$  is the maximal pulling force that the bubble (drop) can resist without detachment. So,  $F_{\text{max}}$  can be used as a quantitative characteristic of the strength of bubble (drop) adhesion to a given substrate. Specific comments on the results shown in the separate panels of Fig. 14 are following.

Fig. 14a shows data for the bubble attachment/detachment process illustrated in Fig. 7. The bubble was manipulated by varying the volume of gas in it (volume control) at fixed distance between the capillary and the substrate. Fig. 14b also corresponds to a bubble in 0.001 wt% HFBII solution, but the bubble was manipulated in a different way – by varying the distance between the capillary and the substrate (distance control), at fixed bubble volume. Experimentally, in the different regimes the volume or the distance has been varied by small steps, which has led to some kinks in the time-dependencies of the investigated parameters. Despite the different dynamics of bubble deformation and different bubble shapes, the obtained values of  $F_{\text{max}}$  are very close: 31.7  $\mu\text{N}$  (Fig. 14a) vs. 33.4  $\mu\text{N}$  (Fig. 14b). Hence,  $F_{\text{max}}$  seems to be a stable characteristic of the strength of bubble adhesion, which is insensitive to the dynamics of bubble manipulation.

For the used experimental setup, the volume control allows a finer manipulation of the bubble than the distance control. For this reason, all other experiments have been carried out under volume control.

Fig. 14c shows results for a bubble in a mixed solution of 0.005 wt% HFBII and 4.8  $\mu\text{M}$  Tween 20. At this relatively low concentration, Tween 20 cannot prevent the solidification of the HFBII layer at the air/water interface. The relatively large value of  $F_{\text{max}}$ , 57.8  $\mu\text{N}$ , and the positive contribution of the disjoining-pressure term,  $-\pi r_c^2 \Pi$ , at the later stages of bubble detachment (Fig. 14c), indicate a stronger adhesion as compared to HFBII alone (Fig. 14a,b). This could be explained with the fact that Tween 20 suppresses the growth of large HFBII aggregates and their attachment to the film surfaces [52]. This allows a closer contact of the two film surfaces and their stronger adhesion. In contrast, in the case of HFBII alone protein aggregates are sandwiched in the films [57, 70]. In such a case, the adhesion of the film surfaces is due mostly to the bridging aggregates, because the close contact of the two surfaces is blocked.

Fig. 14d shows data for mixed solutions of 0.05 wt% PP and 0.005 wt% HFBII. In this case, the bubble surface is always fluid, with isotropic surface tension. For this system, the lowest value of  $F_{\text{max}}$ , 5.6  $\mu\text{N}$ , has been measured from among all investigated systems. The mixing of the two components, PP and HFBII, leads to the appearance of a noticeable turbidity due to the formation of joint aggregates of the two proteins. The low value of  $F_{\text{max}}$  could be attributed to sandwiching of



**Fig. 14.** Comparison of the time dependencies of the external force,  $F_{\text{ext}}$ , transversal tension force,  $2\pi r_c \tau$ , and disjoining pressure force,  $-\pi r_c^2 \Pi$ , acting on bridging bubbles in solutions of (a) 0.001 wt% HFBII – volume control; (b) 0.001 wt% HFBII – distance control; (c) 0.005 wt% HFBII + 4.8  $\mu\text{M}$  Tween 20; (d) 0.05 wt% PP + 0.005 wt% HFBII; (e) 0.05 wt% PP; (f) 0.05 wt% PP + 100 mM NaCl. Note that  $F_{\text{ext}} = 2\pi r_c \tau - \pi r_c^2 \Pi$ . In all cases,  $F_{\text{ext}}$  has a maximum value denoted  $F_{\text{max}}$ , which characterizes the strength of bubble/wall adhesion.

such aggregates in the film, which does not allow the close contact of the two film surfaces. In other words, the mixing of PP and HFBII produces an antagonistic effect on bubble-to-surface adhesion. This effect could be utilized to suppress adhesion if it is undesirable.

Fig. 14e and f present results for 0.05 wt% PP with 0 and 100 mM added NaCl, respectively, at pH = 6.4. In both cases, the bubble surface is fluid, with isotropic surface tension. The values of the maximal adhesive force,  $F_{\text{max}}$ , are among the greatest for the investigated systems. This result could be due to accretion upon contact of the PP adsorption layers formed on the bubble and glass surfaces. The rise of  $F_{\text{max}}$  from 53.9 to 62.7  $\mu\text{N}$  upon the addition of 100 mM NaCl means that the suppression of electrostatic interactions between the protein adsorption layers further enhances the adhesion.

Summarizing the results in Fig. 14, we can conclude that the transversal tension term,  $2\pi r_c \tau$ , is always positive, whereas the disjoining pressure term,  $-\pi r_c^2 \Pi$ , is predominantly negative, with two exceptions – at the final stages of bubble detachment for the solutions with HFBII in Fig. 14a and c. The most important conclusion from Fig. 14 is that the acting external force  $F_{\text{ext}}$  has a maximum, which is the maximal pulling force,  $F_{\text{max}}$ , that the adherent fluid particle can resist. Consequently,

$F_{\text{max}}$  can be used to quantify the *strength of adhesion* of bubbles and drops to solid surfaces. For the investigated systems, the value of  $F_{\text{max}}$  is the greatest, 62.7  $\mu\text{N}$ , for the bubble in the solution of 0.05 wt% PP + 100 mM NaCl (Fig. 14f), and the smallest, 5.6  $\mu\text{N}$ , for the bubble in the mixed solution of 0.05 wt% PP + 0.005 wt% HFBII (Fig. 14d).

### 6.3. Emulsion drop adhesion to surfaces – data analysis

Here, we demonstrate the applicability of the CBD method to another system: adhesion of *emulsion drops* to solid substrates. We investigated a system of practical interest: drops from soybean oil (SBO) in aqueous solutions of 0.01 wt% egg yolk (EY). The adhesion of such drops to substrates from hydrophilic glass, and from glass that had been hydrophobized by HMDS, was studied.

Fig. 15a shows the variation of the capillary pressure,  $p_0$ , determined by the pressure transducer during the detachment of a SBO drop from a *hydrophilic* glass substrate in 0.01 wt% EY solution. Six video frames illustrate the process of drop detachment from the substrate. Fig. 15b presents similar data, but for a substrate of *hydrophobized* glass. In both cases, the drop detachment is carried out under volume control, without

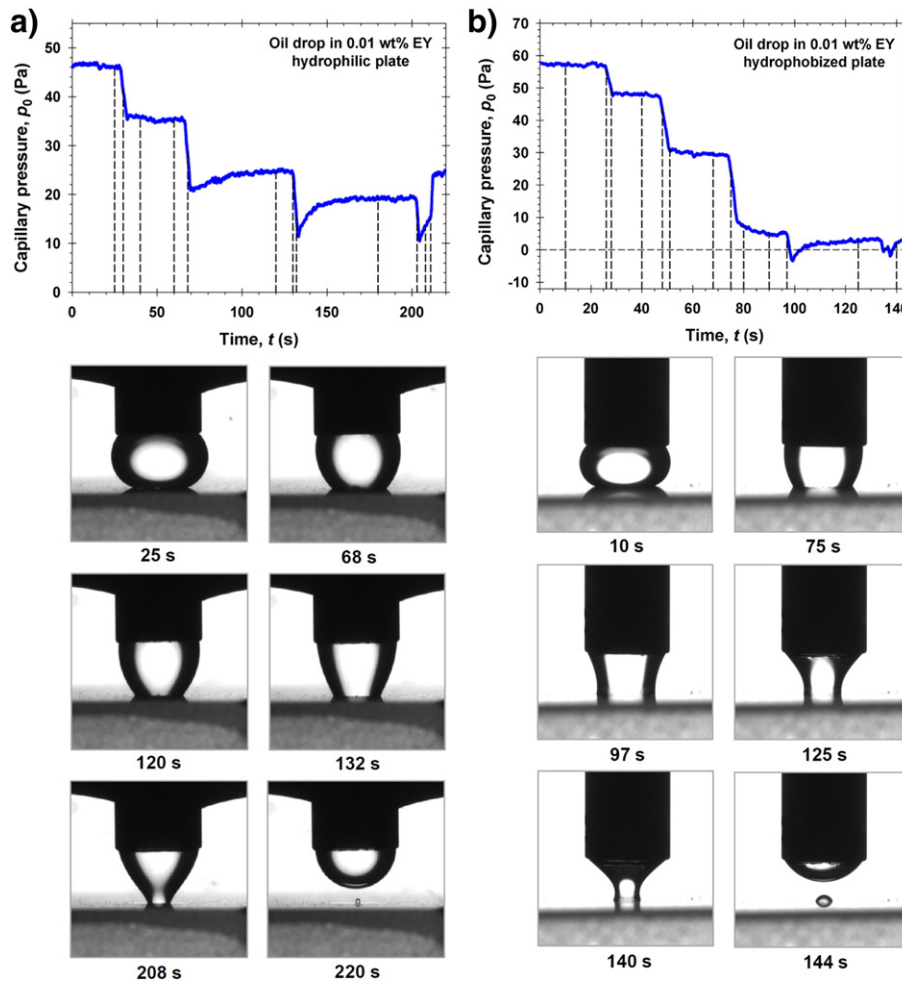


**Fig. 15.** Plot of the capillary pressure,  $p_0$ , vs. time,  $t$ , for an emulsion drop from soybean oil in 0.01 wt% aqueous solution of egg yolk (EY). The vertical dashed lines correspond to the moments of time, at which video frames have been processed; a part of them are shown below the plot of pressure. (a) Hydrophilic glass substrate. (b) Hydrophobized glass substrate.

varying the distance between the capillary and the substrate. As seen in the  $p_0$ -vs.- $t$  plots, the drop volume (and  $p_0$ ) has been decreased in a stepwise manner. Several seconds after the last volume decrease, the

drop detaches from the substrate. In these experiments, the surface tension has been always isotropic, i.e. the interface has been fluid. The vertical dashed lines in the  $p_0$ -vs.- $t$  plots correspond to video frames, which

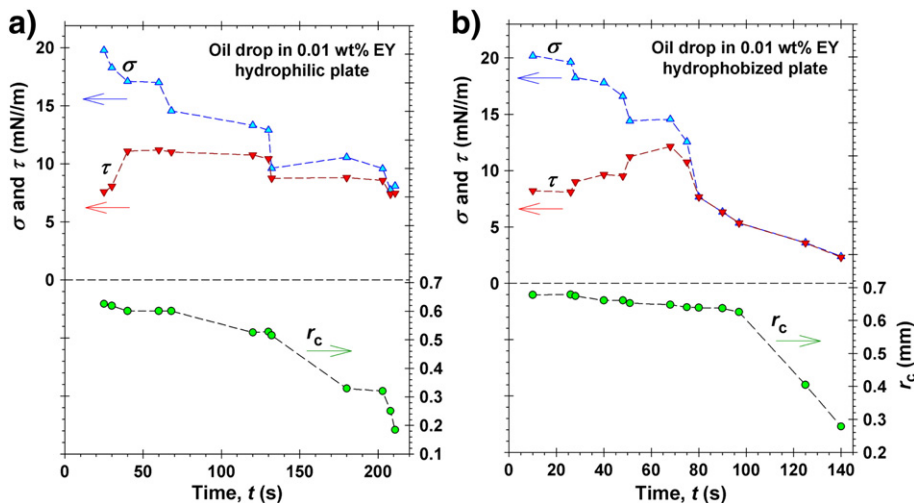


**Fig. 16.** Plots the surface tension  $\sigma$ , transversal tension  $\tau$ , and contact radius  $r_c$  vs. time  $t$  for bridging drops from soybean oil in solutions of 0.01 wt% egg yolk (EY). (a) Hydrophilic glass substrate. (b) Hydrophobized glass substrate.

have been processed by using the CBD procedure to determine  $\sigma$  and  $F$  from the slope and intercept of linear dependencies like that in Fig. 8. The contact radius,  $r_c$ , has been also determined from the digitized drop profile. Then, the transversal tension  $\tau$  is calculated from Eq. (34). Other used relations are  $\Pi = p_0$  and  $F_{\text{ext}} = -F$ .

As seen in the photographs in Fig. 15, in the case of hydrophobized glass plate, the contact angle (measured across water) is systematically greater than that on the hydrophilic substrate, as could be expected. This difference affects also the instantaneous drop profile, which is more concave in the case of hydrophobized substrate. In both cases, a residual drop remains on the substrate after the oil drop detachment. This means that the drop detachment occurs through breakage of the neck of the capillary bridge. (With bubbles, we always observed complete detachment, without residual bubble.) The residual drop is bigger in the case of hydrophobized substrate, as should be expected.

Fig. 16a and b show the experimental dependencies  $\sigma(t)$ ,  $\tau(t)$  and  $r_c(t)$ , for the cases of hydrophilic and hydrophobized glass substrates, respectively. In the case of hydrophilic substrate,  $r_c$  decreases (the drop detaches) more gradually (Fig. 16a). In the case of hydrophobized substrate, initially  $r_c$  decreases slowly, which is followed by a fast detachment during the last stages of the process (Fig. 16b). Because of the relation  $\tau = \sigma \sin \theta_c$ , the difference between  $\tau$  and  $\sigma$  depends on the value of the contact angle  $\theta_c$ . Insofar as the contact line is shrinking,  $\theta_c$  takes instantaneous nonequilibrium values. The initial value of  $\theta_c$  is  $23^\circ - 24^\circ$ , whereas at the final stage of drop detachment  $\theta_c$  reaches maximal values of  $72^\circ$  and  $93^\circ$ , respectively, for the hydrophilic and hydrophobized substrates.

In Fig. 17, we have plotted the external force,  $F_{\text{ext}}$ , which is acting on the drop, and which is counterbalanced by the superposition of the transversal tension force  $2\pi r_c \tau$  (acting on the film periphery) and the disjoining pressure force  $-\pi r_c^2 \Pi$  (acting on the film surface). The transversal tension force is always positive, whereas the disjoining pressure force is negative for the investigated oil drops. As in the case of bubbles, here  $F_{\text{ext}}$  also has a maximal value,  $F_{\text{max}}$ , which is 15.4 and 21.4  $\mu\text{N}$  for the hydrophilic and hydrophobized substrates, respectively.  $F_{\text{max}}$  is greater for the hydrophobized substrate, as it should be expected. The difference between the  $F_{\text{max}}$  values for the two kinds of substrates is not too large. This could be explained with the adsorption of some amounts of EY on both kinds of substrates, which would make their surface properties closer.

## 7. Summary and conclusions

Here, we review the principle and applications of a recently developed method, capillary meniscus dynamometry (CMD), which allows one to determine the surface tension of axisymmetric pendant/buoyant drops and bubbles with both fluid and solidified adsorption layers [27], as well as to quantify the adhesion of such bubbles and drops to solid surfaces. The method uses data for the instantaneous bubble (drop)

profile,  $r(z,t)$ , and capillary pressure,  $p_0(t)$ . The CMD is different from the known drop shape analysis method (DSA) [26] by its procedure for data processing. For DSA, the whole drop/bubble profile is fitted with the Laplace equation by adjusting two parameters, viz. the surface tension  $\sigma$  and the capillary pressure  $p_0$ , using numerical minimization. For CMD, the interface is split to small domains, and the meniscus shape in each domain is fitted with an appropriate quadratic curve. Numerical minimization is not used, so that the CMD computational procedure is fast and can be used to determine the surface-tension dynamics in real time during a given process.

In the more complex case of *solidified* interface (e.g. protein adsorption layer), the bubble (drop) surface tension is anisotropic and has two different components,  $\sigma_s$  and  $\sigma_\varphi$ , which are acting along the “meridians” and “parallels”, and vary throughout the bubble (drop) surface. These two tensions are determined by CMD as functions of the spatial position and time by processing the experimental data using the tangential and normal surface stress balance equations.

In the simpler case of *fluid*, isotropic interface with a constant isotropic surface tension,  $\sigma$ , the procedure is reduced to a fit with linear regression in accordance with Eq. (13). In the case of pendant/buoyant drop or bubble, the slope yields  $\sigma$ , whereas the intercept is zero (Fig. 4a). In the case of bubble or drop pressed against a substrate, which forms a *capillary bridge* (Figs. 7 and 15), the slope yields  $\sigma$ , whereas the intercept yields the capillary-bridge force,  $F$  (Fig. 8). In the case of a capillary bridge with a completely *solidified* surface, meridional *wrinkles* are observed on the bubble (drop) surface. In such a case, the unknown parameter  $F$  can be determined from the intercept of another linear plot; see Fig. 9a.

Two kinds of forces govern the bubble or drop *attachment* to a solid wall (substrate). In most cases, the disjoining pressure force,  $-\pi r_c^2 \Pi$ , that is acting in the thin liquid film (intervening between the bubble/drop and the wall) is repulsive and opposes the bubble/drop adhesion. In contrast, the transversal tension force,  $2\pi r_c \tau$ , acting along the film periphery is always attractive and dominates the adhesion. In other words, the bubble (drop) sticks to the solid surface at its periphery (contact line). The external force acting on the bubble/drop is counterbalanced by the sum of the aforementioned two forces,  $F_{\text{ext}} = 2\pi r_c \tau - \pi r_c^2 \Pi$ . The experiments on bubble/drop detachment show that  $F_{\text{ext}}$  has a maximum, which is the *maximal pulling force*,  $F_{\text{max}}$ , that the adherent fluid particle can resist (Figs. 14 and 17). Consequently,  $F_{\text{max}}$  can be used to quantify the strength of adhesion of bubbles and drops to solid surfaces.

For the various *experimental systems* investigated by us, the greatest  $F_{\text{max}}$  (the strongest bubble adhesion to a hydrophilic glass substrate) was established for *air bubbles* formed in solutions of pea protein (PP) in the presence of 100 mM NaCl. In the case of bubbles in solutions of hydrophobin HFBII,  $F_{\text{max}}$  is about two times smaller, despite the fact that HFBII is known as a “sticky” protein [48,70]. The addition of a small amount of the nonionic surfactant Tween 20 to HFBII leads to an increase of  $F_{\text{max}}$  to values close to those for PP (Fig. 14). A possible

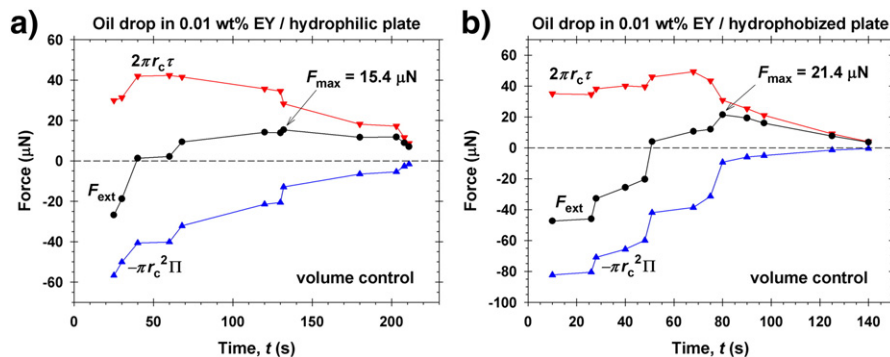


Fig. 17. The same as in Fig. 14, but this time for emulsion drops from soybean oil in aqueous solution of 0.01 wt% egg yolk – see Fig. 15. (a) Hydrophilic glass substrate. (b) Hydrophobized glass substrate. Note that  $F_{\text{ext}} = 2\pi r_c \tau - \pi r_c^2 \Pi$ . In all cases,  $F_{\text{ext}}$  has a maximum value denoted  $F_{\text{max}}$ .

explanation is that Tween 20 suppresses the growth of large HFBII aggregates, which are sandwiched between the bubble and the wall, and prevent the close contact of their surfaces and their stronger adhesion. Big aggregates are formed in the mixed solutions of HFBII and PP, and  $F_{\max}$  is the smallest in this case, which can be explained again with the effect of sandwiched protein aggregates. This effect can be used to suppress the bubble (drop) adhesion to walls, if it is undesirable.  $F_{\max}$  was measured also for oily emulsion drops pressed against hydrophilic and hydrophobized glass substrates in aqueous egg yolk solutions. As expected, the measured  $F_{\max}$  is greater for the hydrophobized substrate.

The results demonstrate that the method of capillary meniscus dynamometry is applicable to both isotropic and anisotropic interfacial adsorption layers. It allows one to determine the surface tension(s), the capillary-bridge force and the maximal pulling force that characterizes the strength of adhesion of bubbles and drops to solid surfaces. The results reveal how the interfacial rigidity and the adhesion force can be quantified and controlled.

## Acknowledgements

The authors gratefully acknowledge the support from Unilever R&D Vlaardingen; from the FP7 project Beyond-Everest, and from COST Actions CM1101, MP1106 and MP1305. The authors are thankful to Prof. Jordan Petkov for the stimulating discussions.

## References

- Pereira LGC, Theodoly O, Blanch HW, Radke CJ. Dilatational rheology of BSA conformers at the air/water interface. *Langmuir* 2003;19:2349–56.
- Freer EM, Yim KS, Fuller GG, Radke CJ. Shear and dilatational relaxation mechanisms of globular and flexible proteins at the hexadecane/water interface. *Langmuir* 2004;20:10159–67.
- Petkov JT, Gurkov TD, Campbell B, Borwankar RP. Dilatational and shear elasticity of gel-like protein layers on air/water interface. *Langmuir* 2000;16:3703–11.
- Borbás R, Murray BS, Kiss E. Interfacial shear rheological behavior of proteins in three-phase partitioning systems. *Colloids Surf A* 2003;213:93–103.
- Krägel J, Derkatch SR, Miller R. Interfacial shear rheology of protein-surfactant layers. *Adv Colloid Interface Sci* 2008;144:38–53.
- Blijdenstein TB, de Groot PWN, Stoyanov SD. On the link between foam coarsening and surface rheology: why hydrophobins are so different. *Soft Matter* 2010;6:1799–808.
- Aumaitre E, Wongsuwan S, Rossetti D, Hedges ND, Cox AR, Vella D, et al. A viscoelastic regime in dilute hydrophobin monolayers. *Soft Matter* 2012;8:1175–83.
- Radulova GM, Golemanov K, Danov KD, Kralchevsky PA, Stoyanov SD, Arnaudov LN, et al. Surface shear rheology of adsorption layers from the protein HFBII hydrophobin: effect of added  $\beta$ -casein. *Langmuir* 2012;28:4168–77.
- Danov KD, Radulova GM, Kralchevsky PA, Golemanov K, Stoyanov SD. Surface shear rheology of hydrophobin adsorption layers: laws of viscoelastic behaviour with applications to long-term foam stability. *Faraday Discuss* 2012;158:195–221.
- Mitropoulos V, Mütze A, Fischer P. Mechanical properties of protein adsorption layers at the air/water and oil/water interface: A comparison in light of the thermodynamical stability of proteins. *Adv Colloid Interface Sci* 2014;206:195–206.
- Evans EA, Skalak R. Mechanics and thermodynamics of biomembranes. *CRC Crit Rev Bioeng* 1979;3:181–330.
- Rosenfeld L, Cerretani C, Leiske DL, Toney MF, Radke CJ. Structural and rheological properties of meibomian lipid. *Invest Ophthalmol Vis Sci* 2013;54:2720–32.
- Hermans E, Vermant J. Interfacial shear rheology of DPPC under physiologically relevant conditions. *Soft Matter* 2014;10:175–86.
- Espinosa G, Langevin D. Interfacial shear rheology of mixed polyelectrolyte – surfactant layers. *Langmuir* 2009;25:12201–7.
- Arriaga LR, Monroy F, Langevin D. The polymer glass transition in nanometric films. *Europhys Lett* 2012;98:38007.
- Humblet-Hua NPK, van der Linden E, Sagis LMC. Surface rheological properties of liquid-liquid interfaces stabilized by protein fibrillar aggregates and protein-polysaccharide complexes. *Soft Matter* 2013;9:2154–65.
- Stanimirova R, Marinova K, Tcholakova S, Denkov ND, Stoyanov S, Pelan E. Surface rheology of saponin adsorption layers. *Langmuir* 2011;27:12486–98.
- Zang DY, Rio E, Langevin D, Wei B, Binks BP. Viscoelastic properties of silica nanoparticle monolayers at the air-water interface. *Eur Phys J E* 2010;31:125–34.
- Fuller GG, Vermant J. Complex fluid-fluid interfaces: rheology and structure. *Annu Rev Chem Biomol Eng* 2012;3:519–43.
- Fan Y, Simon S, Sjöblom J. Interfacial shear rheology of asphaltene at oil-water interface and its relation to emulsion stability: Influence of concentration, solvent aromaticity and nonionic surfactant. *Colloids Surf A* 2010;366:120–8.
- Long R, Shull KR, Hui CY. Large deformation adhesive contact mechanics of circular membranes with a flat rigid substrate. *J Mech Phys Solids* 2010;58:1225–42.
- Carvajal D, Laprade EJ, Henderson KJ, Shull KR. Mechanics of pendant drops and axisymmetric membranes. *Soft Matter* 2011;7:10508–19.
- Ferri JK, Fernandes PAL, McRuiz JT, Gambinossi F. Elastic nanomembrane metrology at fluid-fluid interfaces using axisymmetric drop shape analysis with anisotropic surface tensions: deviations from Young-Laplace equation. *Soft Matter* 2012;8:10352–9.
- Laprade EJ, Long R, Pham JT, Lawrence J, Emrick T, Crosby AJ, et al. Large deformation and adhesive contact studies of axisymmetric membranes. *Langmuir* 2013;29:1407–19.
- Knoche S, Vella D, Aumaitre E, Degen P, Rehage H, Cicuta P, et al. Elastometry of deflated capsules: Elastic moduli from shape and wrinkle analysis. *Langmuir* 2013;29:12463–71.
- Rotenberg Y, Boruvka I, Neumann AW. Determination of surface tension and contact angle from the shapes of axisymmetric fluid interfaces. *J Colloid Interface Sci* 1983;93:169–83.
- Danov KD, Stanimirova RD, Kralchevsky PA, Marinova KG, Alexandrov NA, Stoyanov SD, et al. Capillary meniscus dynamometry – Method for determining the surface tension of drops and bubbles with isotropic and anisotropic surface stress distributions. *J Colloid Interface Sci* 2015;440:168–78.
- Bashforth F, Adams C. An attempt to test the theories of capillary action. Cambridge: Cambridge Univ Press; 1892.
- Andreas JM, Hauser EA, Tucker WB. Boundary tension by pendant drops. *J Phys Chem* 1938;42:1001–19.
- Rusanov AI, Prokhorov VA. Interfacial tensiometry. Amsterdam: Elsevier; 1996.
- Ferri JK, Lin SY, Stebe KJ. Curvature effects in the analysis of pendant bubble data: Comparison of numerical solutions, asymptotic arguments, and data. *J Colloid Interface Sci* 2001;241:154–68.
- Zholob SA, Makievski AV, Miller R, Fainerman VB. Optimisation of calculation methods for determination of surface tensions by drop profile analysis tensiometry. *Adv Colloid Interface Sci* 2007;134:322–9.
- Ravera F, Loglio G, Kovalchuk VI. Interfacial dilatational rheology by oscillating bubble/drop methods. *Curr Opin Colloid Interface Sci* 2010;15:217–28.
- Hoorfar M, Neumann AW. Recent progress in axisymmetric drop shape analysis (ADSA). *Adv Colloid Interface Sci* 2006;121:25–49.
- Kalantarian A, Saad SMI, Neumann AW. Accuracy of surface tension measurement from drop shapes: The role of image analysis. *Adv Colloid Interface Sci* 2013;199–200:15–22.
- Saad SMI, Neumann AW. Total Gaussian curvature, drop shapes and the range of applicability of drop shape techniques. *Adv Colloid Interface Sci* 2014;204:1–14.
- Passerone A, Liggieri L, Rando N, Ravera F, Ricci E. A new experimental method for the measurement of the interfacial tension between immiscible fluids at zero Bond number. *J Colloid Interface Sci* 1991;146:152–62.
- MacLeod CA, Radke CJ. A growing drop technique for measuring dynamic interfacial tension. *J Colloid Interface Sci* 1993;160:435–48.
- Nagarajan R, Wasan DT. Measurement of dynamic interfacial tension by an expanding drop tensiometer. *J Colloid Interface Sci* 1993;159:164–73.
- Johnson DO, Stebe KJ. Oscillating bubble tensiometry: a method for measuring the surfactant adsorptive-desorptive kinetics and the surface dilatational viscosity. *J Colloid Interface Sci* 1994;168:21–31.
- Javadi A, Krägel J, Karbaschi M, Won J, Dan A, Gochev G. Capillary pressure experiments with single drops and bubbles. In: Kralchevsky P, Miller R, Ravera F, editors. *Colloid and interface chemistry for nanotechnology*. CRC Press: Boca Raton; 2014. p. 271–312. <http://crncbase.com/doi/abs/10.1201/b15262-16>.
- Russev SC, Alexandrov N, Marinova KG, Danov KD, Denkov ND, Lyutov L, et al. Instrument and methods for surface dilatational rheology measurements. *Rev Sci Instrum* 2008;79:104102.
- Georgieva D, Cagna A, Langevin D. Link between surface elasticity and foam stability. *Soft Matter* 2009;5:2063–71.
- Javadi A, Krägel J, Makievski AV, Kovalchuk NM, Kovalchuk VI, Mucic N, et al. Fast dynamic interfacial tension measurements and dilatational rheology of interfacial layers by using the capillary pressure technique. *Colloids Surf A* 2012;407:159–68.
- Eliassen JD. *Interfacial mechanics*. Ph.D. Thesis, University of Minnesota, 1963. Ann Arbor, MI: University Microfilms; 1983.
- Kralchevsky PA, Eriksson JC, Ljunggren S. Theory of curved interfaces and membranes: mechanical and thermodynamical approaches. *Adv Colloid Interface Sci* 1994;48:19–59.
- Kralchevsky PA, Nagayama K. Particles at fluid interfaces and membranes. Amsterdam: Elsevier; 2001[Chapters 2–5 and 11].
- Linder MB. Hydrophobins: proteins that self assemble at interfaces. *Curr Opin Colloid Interface Sci* 2009;14:356–63.
- Zhang XL, Penfold J, Thomas RK, Tucker JM, Petkov JT, Bent J, et al. Adsorption behavior of hydrophobin and hydrophobin/surfactant mixtures at the air-water interface. *Langmuir* 2011;27:11316–23.
- Alexandrov NA, Marinova KG, Gurkov TD, Danov KD, Kralchevsky PA, Stoyanov SD, et al. Interfacial layers from the protein HFBII hydrophobin: Dynamic surface tension, dilatational elasticity and relaxation times. *J Colloid Interface Sci* 2012;376:296–306.
- Stanimirova RD, Marinova KG, Danov KD, Kralchevsky PA, Basheva ES, Stoyanov SD, et al. Competitive adsorption of the protein hydrophobin and an ionic surfactant: Parallel vs sequential adsorption and dilatational rheology. *Colloids Surf A* 2014;457:307–17.
- Danov KD, Kralchevsky PA, Radulova GM, Basheva ES, Stoyanov SD, Pelan EG. Shear rheology of mixed protein adsorption layers vs their structure studied by surface force measurements. *Adv Colloid Interface Sci* 2015. <http://dx.doi.org/10.1016/j.cis.2014.04.009>.
- Radulova GM, Danov KD, Kralchevsky PA, Petkov JT, Stoyanov SD. Shear rheology of hydrophobin adsorption layers at oil/water interfaces and data interpretation in terms of a viscoelastic thixotropic model. *Soft Matter* 2014;10:5777–86.

- [54] Krägel J, Wüstneck R, Husband F, Wilde PJ, Makievski AV, Grigoriev DO, et al. Properties of mixed protein/surfactant adsorption layers. *Colloids Surf B* 1999;12:399–407.
- [55] Kovacs-Nolan J, Phillips M, Mine Y. Advances in the value of eggs and egg components for human health. *J Agric Food Chem* 2005;53:8421–31.
- [56] Danov KD, Kralchevsky PA, Stoyanov SD. Elastic Langmuir layers and membranes subjected to unidirectional compression: wrinkling and collapse. *Langmuir* 2010;26:143–55.
- [57] Basheva ES, Kralchevsky PA, Christov NC, Danov KD, Stoyanov SD, Blijdenstein TBJ, et al. Unique properties of bubbles and foam films stabilized by HFBII hydrophobin. *Langmuir* 2011;27:2382–92.
- [58] Aumaitre E, Knoche S, Cicuta P, Vella D. Wrinkling in the deflation of elastic bubbles. *Eur Phys J E* 2013;36:22.
- [59] Derjaguin BV, Churaev NV. On the question of determining the concept of disjoining pressure and its role in the equilibrium and flow of thin films. *J Colloid Interface Sci* 1978;66:389–98.
- [60] Kralchevsky PA, Ivanov IB. On the mechanical equilibrium between a film of finite thickness and the external meniscus. *Chem Phys Lett* 1985;121:111–5.
- [61] Kralchevsky PA, Ivanov IB. The transition region between a thin film and the capillary meniscus. *Chem Phys Lett* 1985;121:116–21.
- [62] Israelachvili JN. *Intermolecular and surface forces*. London: Academic Press; 2011.
- [63] Derjaguin BV. *Theory of stability of colloids and thin films*. New York: Springer; 1989.
- [64] Hammer MU, Anderson TH, Chaimovich A, Shell MS, Israelachvili J. The search for the hydrophobic force law. *Faraday Discuss* 2010;146:299–308.
- [65] Kralchevsky PA, Danov KD, Ivanov IB. Thin liquid film physics. In: Prud'homme RK, Khan SA, editors. *Foams: theory, measurements and applications*. New York: Marcel Dekker; 1995. p. 1–97.
- [66] Kralchevsky PA, Danov KD, Denkov ND. Chemical physics of colloid systems and interfaces. In: Birdi KS, editor. *Handbook of surface and colloid chemistry*. Boca Raton: CRC Press; 2008. p. 197–377. <http://dx.doi.org/10.1201/9781420007206.ch7>.
- [67] Nikolov AD, Kralchevsky PA, Ivanov IB, Dimitrov AS. Differential interferometric investigation of curved liquid films. In: Krantz WB, Wasan DT, Jain RK, editors. *Thin liquid film phenomena*. 82. AIChE Symposium Series; 1986. p. 82–90.
- [68] Gurkov TD, Kralchevsky PA. Mechanics and thermodynamics of interfaces, thin liquid films and membranes. *J Dispers Sci Technol* 1997;18:609–23.
- [69] Stanimirova RD, Gurkov TD, Kralchevsky PA, Balashev KT, Stoyanov SD, Pelan EG. Surface pressure and elasticity of hydrophobin HFBII layers on the air-water interface: rheology versus structure detected by AFM imaging. *Langmuir* 2013;29:6053–67.
- [70] Basheva ES, Kralchevsky PA, Danov KD, Stoyanov SD, Blijdenstein TBJ, Pelan EG, et al. Self-assembled bilayers from HFBII hydrophobin: nature of the adhesion energy. *Langmuir* 2011;27:4481–8.